A NUMERICAL STUDY FOR AERODYNAMIC PERFORMANCES OF NREL OFFSHORE 5-MW WIND TURBINE
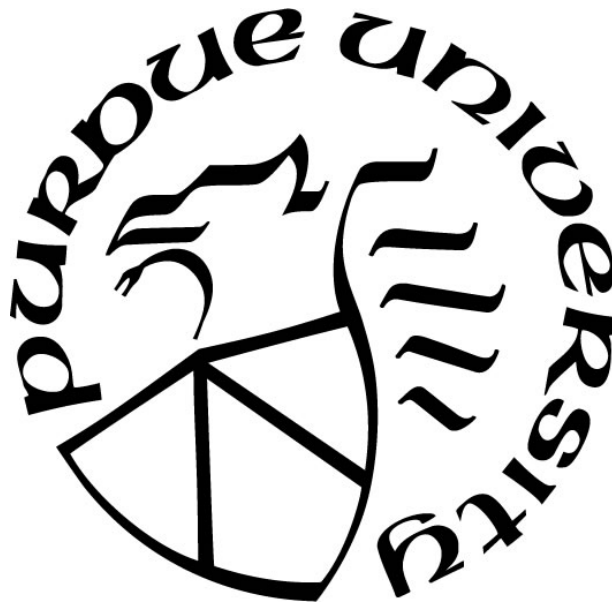
by

Qiqing Zhang

A Thesis

Submitted to the Faculty of Purdue University

In Partial Fulfillment of the Requirements for the degree of

Master of Science in Engineering

Department of Electrical and Computer Engineering

Hammond, Indiana

August 2021

THE PURDUE UNIVERSITY GRADUATE SCHOOL
STATEMENT OF COMMITTEE APPROVAL

Dr. Xiuling Wang, Chair

Department of Mechanical and Civil Engineering

Dr. Hansung Kim

Department of Mechanical and Civil Engineering

Dr. Yun (Tom) Liu

Department of Mechanical and Civil Engineering

Approved by:

Dr. Chenn Q. Zhou

ACKNOWLEDGMENTS

TABLE OF CONTENTS

LIST OF TABLES

LIST OF FIGURES

NOMENCLATURE

a   axial induction factor

a'   angular induction factor

B   number of blades

C   chord thickness

C_l lift coefficient

C_d drag coefficient.

c   chord length of wind turbine blade

$C_{1\varepsilon}$ constant 1.44

C_2 constant 1.9

C_p power coefficient

P_∞ pressure at infinity = 0

P_0 total pressure

Q   second invariant velocity gradient tensor

r   radius coordinate

R   radius of the blade = 62.9 m

S_k user-define source term

S_ε user-define source term

S_{ij} rate of strain tensor

t time

U   wind speed

U_{hub} velocity at hub height

U_{ref} reference velocity

$u(z)$ wind velocity at certain height z

z certain height

λ tip speed ratio

α wind shear exponent

Ω_{ij} vorticity tensor

ρ air density

μ viscosity

ε turbulence dissipation rate

ABSTRACT

Wind energy is recognized as a sustainable source of energy that is both reliable and capable of dramatically reducing pollution to the environment and dependency on non-renewable fuels, leading to research on wind turbines. Nowadays, the demand for electricity increases. Considering that the greater the distance from shore, the greater the wind, more electricity will be generated along the coast. It is necessary and beneficial to study large scale offshore wind turbines. The National Renewable Energy Lab (NREL) 5-MW offshore wind turbine is simulated using a three-dimensional computational fluid dynamics (CFD) model in this article. A realizable k-ε viscous model is used to simulate turbulence flow. The work is validated by comparing the torque with published simulated data, and satisfied consistency is observed. Further simulation and comprehensive analysis demonstrate the flow features and aerodynamic performances of 5-MW offshore wind turbine under various wind and rotor speeds. The velocity profiles, total pressure distribution, pressure coefficient, rotor thrust, torque and aerodynamic properties are obtained in detail.

1. INTRODUCTION

1.1 Background and Motivation

Wind energy is amongst the most appealing energy sources since it is the cleanest, most cost-effective source of energy [1], especially considering the environment and growing popularity of renewable energy [2]. The use of wind energy can be traced back to 200 BC in China, it was utilized to move the gears of mills acting as the driving force to pump water [3]. Hundreds of years later, wind power can be transformed into electricity which is attributed to the emergence of wind turbines. In 2018, global capacity of wind power reached over 600GW. China contributes 221GW, or more than one-third of global capacity, and is unquestionably the leading country in wind energy. Gansu Province in China is home to the world's greatest onshore windfarm, which is five times larger than its next competitor, the Alta Wind Energy Centre in California, which is home to the world's second biggest onshore windfarm in states. Despite having 96.4GW of power generation, the United States is competitive in onshore wind power. Six out of every ten onshore wind farms are in the states. More than 800 GW of wind generating capacity is anticipated to be built globally by 2020 [4] [5].

There is no doubt that wind energy is environmentally friendly and renewable that does not require combustion and does not emit greenhouse gases. According to research published by National Renewable Energy Institute (NREL), 1MW of wind power could prevent the release of 2,600 tons of carbon from fossil fuels. Wind turbines can be installed in unproductive land, mountainous and desert areas, fertile land, sloping land, and even coastal areas. They can not only be placed in unproductive land, but also in land with other use. For example, they can coexist with land that is used to raise cattle, and plant low-lying crops like wheat, beets, corn. What's more, the use of wind turbines can be combined with other kinds of energy, such as solar energy, so it is able to offer an energy autonomy to buildings. Using wind turbines to generate electricity is also a good way to supply energy for remote areas. Nowadays, considering the shortage of resources, the growth of population, the electricity demand for is explosively growing. The best places for wind farms are in coastal and offshore areas, where the wind is stronger and more uniformly [6]. The greater the distance from shore, the greater the wind, more electricity will be generated along the coast. Thus, it is necessary and beneficial to study large scale offshore wind turbines. Among

numerous large scale wind turbines, 5 MW offshore wind turbine from NREL for offshore system is selected to be analyzed since plenty of experimental and numerical data is available and a large amount of research have been done.

1.2   Literature Review

Nowadays, both experimental and numerical approaches are in use for complicated onshore and offshore wind turbine analysis.

Several experimental studies had been designed to investigate the behavior of onshore wind turbines. In 2015, a test was carried out by Wenehenubun et al. [7], to analyze the influence of the amount of blades on the model of a Savonius wind turbine in Atma Jaya Catholic University. They compared the aerodynamic features of wind turbines with two, three, and four blades. They also stated that the model with three blades outperformed the others in terms of high speed ratio. In addition, Huang et al. [8] investigated the protuberance impact on a variable-speed wind turbine in 2015. They came to the conclusion that protuberant blades with lower amplitudes performed better in the stall area. More recently, Talavera et al. [9] tested a single wind turbine model with two blades under different inflow conditions. They observed that the coefficient of power was strongly linked to the intensity of flow.

Recently, the dynamic performance of several offshore wind turbine designs under diverse environmental circumstances was investigated through a series of experimental tests. Coulling et al., 2013 [10] used a 1/50-scale model of an NREL 5-MW offshore wind turbine constructed for a floating platform to verify a model from FAST. They analyzed the performance in terms of elasticity, aerodynamics, and hydrodynamics, compared test results to FAST predictions, and discovered that FAST and test achieved a high level of agreement. Shin et al., 2014 [11] constructed a 1/128-scale model of a 5-MW floating offshore wind in a water depth of 50 m in the University of Ulsan's Ocean Engineering Wide Tank. The response amplitude operator in natural frequency was produced and compared under various situations. Duan et al., 2016 [12] simulated a test to examine the dynamical reaction of an OC3 model of spar floating wind turbine at 1/50 scale. They also documented the reaction behavior under wind and wave conditions. These investigations were meticulously planned and carried out in order to provide references for simulation research.

To satisfy the requirement of forecasting dynamic performances of onshore wind turbines, a numerical technique that was more cost-effective than experimental testing stood out. Troldborg et al. [13] utilized the Navier-Stokes solver EllipSys3D to model the wake interaction between two 2-MW NM80 turbines in onshore wind turbine study.

It is well known that experimental modeling experiments were costly. Furthermore, satisfying platform testing using Froude scaling and for large-scale offshore wind turbines using Reynolds scaling at the same time was unfeasible. Inaccuracy would be developed when the test findings were applied to full-scale wind turbines. Cheng et al. [14] investigated the aerodynamic and hydrodynamic responses of an NREL 5-MW offshore wind turbine placed on a semi-submersible foundation using OpenFOAM. Zhou et al. [15] analyzed the aerodynamic behaviors of the 5-MW offshore wind turbine in downwind and upstream settings using the PimpleDyMFoam solver based on OpenFOAM. Wake vortices, pressure distributions on the blade, and limiting streamlines were analyzed. Cheng et al. also [16] also investigated the unstable aerodynamic characteristics of NREL-5MW offshore wind turbine with periodic pitch and surge movements of the platform using the naoe-FOAM-SJTU technique based on OpenFOAM. They also demonstrated that compared with surge motion pitch motion had a greater effect on the the thrust and torque of the rotor.

NREL created a comprehensive design of a 5 MW offshore wind turbine in 2009, which had been utilized for aerodynamic research. [17]. Moreover, it was also an accurate representation of the features of a conventional 5 MW offshore wind turbine. Furthermore, in modern society, output power of major wind turbines was in the range from 3.6 to 6 MW [18]. As a result, it was chosen for this job.

The capacity of an offshore wind turbine was impacted by its aerodynamic performance. Considering that higher capacity is required, the behavior of aerodynamic performance should be better. Thus, aerodynamic performance was substantial for offshore wind turbine design, and plenty of research on aerodynamic behaviors of 5-MW offshore wind turbine had been done.

It was difficult to discuss the aerodynamic behaviors directly, taking account the fact that 5-MW offshore wind turbine had 6 degrees of freedom. Therefore, firstly analyzing the aerodynamic performance without considering the floating structures was a better way. Wang [19] utilized the CFD approach to describe the three-dimensional transient flow for an offshore 5-MW wind turbine at 9 m/s. The contours of velocities and pressure were presented. He calculated the

wind turbine aerodynamic torque efficiency to be 72.2% using LES model and concluded that LES method was a reliable tool to study complex transient turbulent flows. The multiple reference frame (MRF) technique, which is based on OpenFOAM, was used by Zhao et al. [24] to simulate a 5-MW offshore wind turbine at varying wind speeds. They obtained the aerodynamic features on the blade surfaces and got the wake vortex, rotor thrust, and torque without taking into account the effect of the floating structure. The aerodynamic performance of a selected 5-MW offshore baseline wind turbine at the mouth of the Chesapeake Bay was modelled by Aquino [26]. They calculated the lift coefficient, drag coefficient, tangential velocity, axial velocity, and AOA at different inlet wind velocities along the azimuth and blades.

When it came to offshore wind turbines with additional 6 degrees of freedom motions, which means the wind turbine id floating, the aerodynamic behaviors and flowfield around the rotor blades were more complex. Lienard et al. [20] used CFD to examine the aerodynamic behavior of a 5-MW offshore wind turbine under various wave movements. According to their findings, pitch and surge movements had a significant impact on boosting mean aerodynamic power among 6 degrees of freedom motions. Tran et al. [21] demonstrated a floating wind turbine device with a periodic pitch motion. They completed the spinning turbine's unsteady aerodynamic study satisfactorily. The effects of platform movements on aerodynamic performance were examined by Lee et al. [22]. They tested the 5-MW offshore wind turbine with periodic translational and rotational movements and compared the results to the bottom-fixed simulation. The result they reached also suggested that surge and pitch motions had a major impact on thrust and power, which was similar to Lienard et al. [20] and Cheng et al. [16].

In addition to the aerodynamic performances, aeroelastic behaviors of rotor blades were vital to offshore 5-MW wind turbines. Dose et al. [23] coupled OpenFoam with BeamFoam to investigate the areo-elastic behavior of NREL 5-MW offshore baseline wind turbine. The effect of blade deformations on power, thrust and sectional forces were presented. They pointed out that the aerodynamic performances were influenced clearly by structural deformations. The aeroelastic response was investigated using a combined CFD-CSD technique by Dong et al. [25]. They began by comparing stable blade bending and average rotor loads to other expected findings. Unsteady blade deformation and loads were then examined. They concluded that the aeroelastic blade deformation considerably lowered the loads on the blades, and that the unsteady dynamic load behaviors were also altered.

Obviously, several studies on the aerodynamic behavior of a 5-MW offshore baseline wind turbine have been conducted. Some investigated the aerodynamic performance under the condition that inlet wind velocity is less than the rated wind speed, some may only put emphasis on the behaviors at the rated wind speed. Few research was about the aerodynamic performance under three different conditions. Therefore, the work presented in this paper demonstrated a comprehensive study on aerodynamic behavior of 5-MW offshore wind turbine at three different conditions.

2. AERODYNAMICS OF WIND TURBINE

2.1 Aerodynamic Features

The aerodynamic features which are further discussed in the following chapters are introduced in this section.

The given formula may be implemented to calculate the pressure coefficient [24].

$$pressure\ coefficient = \frac{2(P_0 - P_\infty)}{\rho(U^2 + (\omega r)^2)} \tag{1}$$

Where P_∞ is the pressure at infinity, which is set as 0, P_0 is the total pressure, and the wind speed is denoted by the letter U. ω is the angular velocity in rad/s, r is the radius coordinate of the wind turbine.

Tip speed ratio, which is the ratio of tangential tip velocity to wind velocity, is an essential metric in turbine design. Tangential tip velocity is described as

$$V_t = \omega r \tag{2}$$

Therefore, the tip speed ratio can be expressed as

$$TSR = \lambda = \frac{\omega r}{v} \tag{3}$$

The coefficient of power is also a significant parameter in wind turbine study. It is expressed as the following equation.

$$C_p = \frac{power\ generated}{1/2\ \rho A v^3} \tag{4}$$

Where A is the sweeping area of the wind turbine. And A is known as

$$A = \pi R^2$$

R is the distance from the center of the hub to the blade tip, here R is 62.9 m.

The power generated is described as

$$Power = T\omega \tag{5}$$

Thus, the power coefficient is also expressed as

$$C_p = \frac{T\omega}{1/2\ \rho \pi r^2 v^3} \tag{6}$$

Where, T is the torque, ρ is the density of the air, here the air density equals to 1.225 kg/m³, v is the inlet wind velocity.

16

The power coefficient is expressed as the following equation as well

$$C_p = 4a(1-a)^2 \tag{7}$$

Where, a is the axial induction factor.

By differentiating equation above, the maximum theoretically possible rotor power occurs at

$$\frac{dC_p}{da} = 3a^2 - 4a + 1 = 0 \tag{8}$$

Which makes a = 1/3, and $C_{pmax} = 0.59$.

Thus, the maximum theoretical power coefficient is no more than 0.59.

2.2   Aerodynamic Models

Blade Element Momentum theory (BEM) and Computational Fluid Dynamic method are commonly used to simulate the aerodynamic features of wind turbines. BEM method is the oldest method for providing reasonable estimates of turbine analysis [17][19]. However, since it relies on the airfoil data significantly, the accuracy of aerodynamic calculation will be affected. On the other side, CFD method is an attractive and powerful method to obtain flow and aerodynamic features. In this section, both BEM theory and CFD method will be introduced.

2.2.1   BEM theory

It has been a long history since the raise of blade momentum theory. BEM theory is refined by Betz and Glauert [29] and it is the unite of the blade element theory and momentum theory. BEM method divides the certain blade into several elements along the span direction. These elements are analyzed as two-dimensional airfoils and the aerodynamic features such as thrust, and torque of the airfoil could be calculated. By integrating the whole elements, the aerodynamic features of the whole blade can be deducted. The thrust on each airfoil is expressed as [28]

$$dT = \frac{1}{2}B\rho C\left(V_W{}^2(1-a)^2 + \omega^2 r^2(1+a')^2\right)(C_l \cos\varphi + C_d \sin\varphi)dr \tag{9}$$

And the torque on each airfoil is described as

$$dQ = \frac{1}{2}B\rho Cr\left(V_W{}^2(1-a)^2 + \omega^2 r^2(1+a')^2\right)(C_l \sin\varphi - C_d \cos\varphi)dr \tag{10}$$

17

where a' is the angular induction factor, B refers the number of blades, C is the chord thickness, C_l is coefficient of lift and C_d refers to the drag coefficient.

In order to connect the velocities with the force mentioned above, the formulas for thrust and torque based on momentum theory in a stream tube are used and expressed as

$$dT = 4\pi r \rho V_W{}^2 a(1-a)dr \tag{11}$$

$$dQ = 4\pi r^3 \rho V_W{}^2 a'\omega(1-a)dr \tag{12}$$

Since calculation using BEM method is not complicated, the requirement for computational computer is not demanding, even any office type computers could be qualified. However, it is also its simplicity that creates some shortcomings. One of the weaknesses is that the airflow around the airfoil is considered as be in equilibrium all the time during the calculation. The flow could adjust immediately based on the change of vorticity. But in real life, it will cost some time for the passing flow to adjust. The other disadvantage is that the forces applied on the airfoils are deemed as two-dimensional. Thud, the force caused by the flow in the spanwise direction is ignored.

2.2.2 CFD methods

Unlike BEM theory, CFD methods are able to solve unsteady flow and could visualize the aerodynamic features such as pressure distribution and wake vortex. Two turbulent methods are widely implemented for wind turbine analysis. Reynolds-averaged Navier–Stokes (RANS) is one of the oldest methods of turbulence. The physical parameter of a fluid motion can be expressed as the sum of the fluctuating part and the mean part. Substituting the new expression into the original N-S equation and then averaging it, the RANS equation can be obtained. Nowadays, k-ε model and k-omega model are commonly applied. The other turbulent method is LES model. LES filters small eddies and only simulates the large eddies. It has a better depiction of turbulence in the aspect of wind turbine simulation, but finer mesh is required for LES model, which leads to more computational resources.

3. METHODOLOGY

3.1 Wind Turbine Geometry

In this paper, NREL 5-MW offshore baseline wind turbine [17] was picked up for the simulation. The wind turbine features a 129-meter-diameter blade with a radius of roughly 63 meters. It is a wind turbine with three blades. The cut in velocity, rated velocity, and cut-out velocity are 3 m/s, 11.4 m/s and 25 m/s, respectively.

Table 1 demonstrates the aerodynamic characteristics of the blade nodes placed at the center of the blade element. Each node represents different cross section from the center of the turbine. Take node 6 as an example, the distance from the center of the turbine to it is 19.95 m. The chord length of the airfoil at the plane is 4.46 m and the twist of the blade is 10.16 degrees. It will also use the DU35 airfoil.

Table 1. Distributed Blade Aerodynamic Properties

Node	RNodes (m)	AeroTwst (deg.)	Chord (m)	Airfoil
1	2.87	13.31	3.54	Circle1
2	5.60	13.31	3.85	Circle1
3	8.33	13.31	4.17	Circle2
4	11.75	13.31	4.56	DU40
5	15.85	11.48	4.65	DU35
6	19.95	10.16	4.46	DU35
7	24.05	9.01	4.25	DU30
8	28.15	7.80	4.01	DU25
9	32.25	6.64	3.75	DU25
10	36.35	5.36	3.50	DU21
11	40.45	4.19	3.26	DU21
12	44.55	3.13	3.01	NACA64
13	48.65	2.32	2.76	NACA64
14	52.75	1.53	2.52	NACA64
15	56.17	0.86	2.31	NACA64
16	58.90	0.37	2.09	NACA64
17	61.63	0.11	1.42	NACA64

Various airfoils are used according to Table 1. Three cylinders are used at the root of the blade and DU series airfoils are used in the middle part of the turbine blade. With the decrease of the chord, NACA 64 airfoil is used all along to the blade tip. All the airfoil profiles mentioned in Table 1 are described in Figure 1.
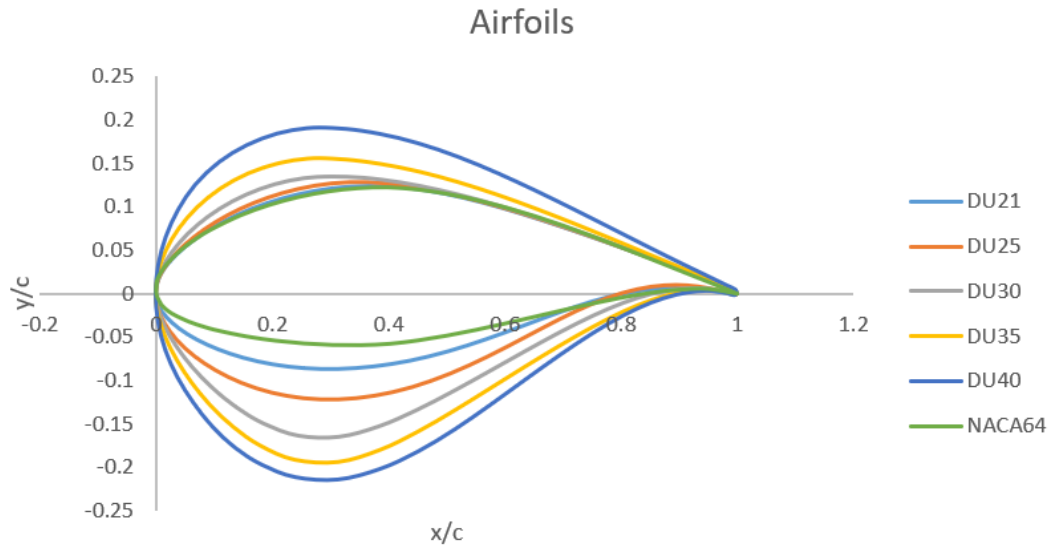
Figure 1. Airfoil cross-sections used in turbine design

Based on the information presented above, the geometry model of the wind turbine can be generated using Solidworks. The airfoils at various cross sections are exhibited in Figure 2. The geometry of the wind turbine blade is presented in Figure 3. Assemble the turbine blades and the hub together, the geometry of the 5MW offshore wind turbine is obtained in Figure 4.
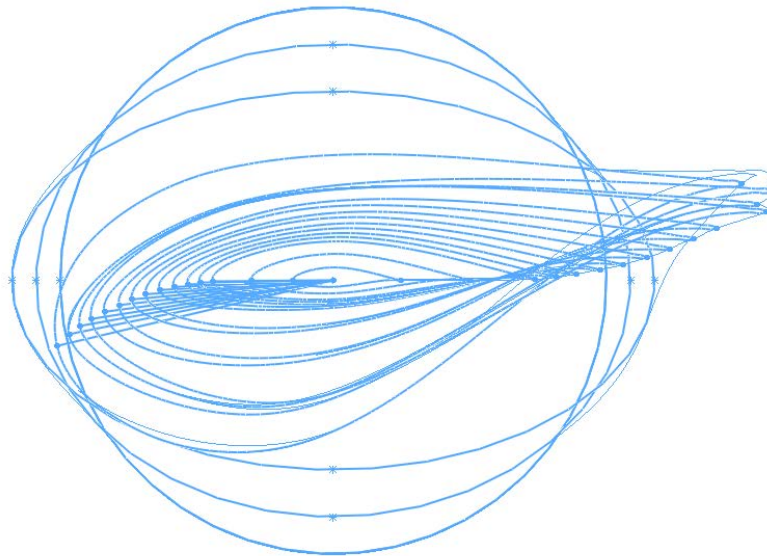

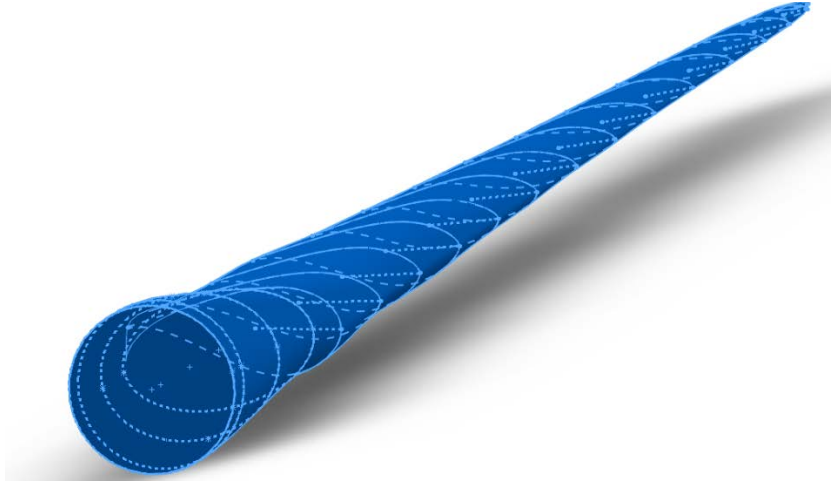Figure 2. Airfoils of wind turbine blade

Figure 3. Geometry of wind turbine blade
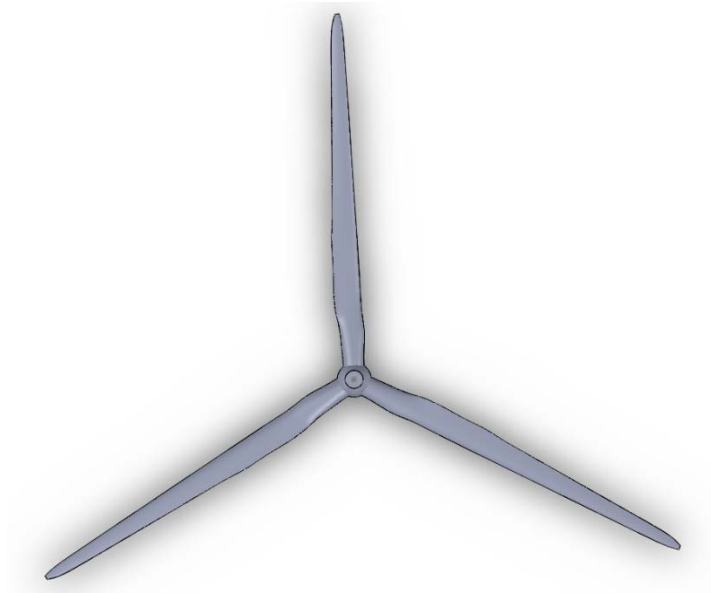
Figure 4. Geometry of the whole wind turbine

3.2   Mesh Generation and Mesh Independent Study

Medium mesh is demonstrated in Figure 5. It is vital to generate fine mesh for the computational domains since the quality of mesh played an important role on the simulation results. The whole domain contains 2,479,240 cells. In this work, the first objective is to obtain the torque of the wind turbine, so the mesh near the wind turbine blades and rotor are significant. Considering the fact that the scale of the whole computational domain was quite large, the computational time

would be large if extremely small meshes were applied to the whole computational domain. Body sizing was inserted on the whole fluid computational domain and rotating domain. Edge sizing was inserted on turbine side and tip edges so as to obtain finer meshes for more accurate results.
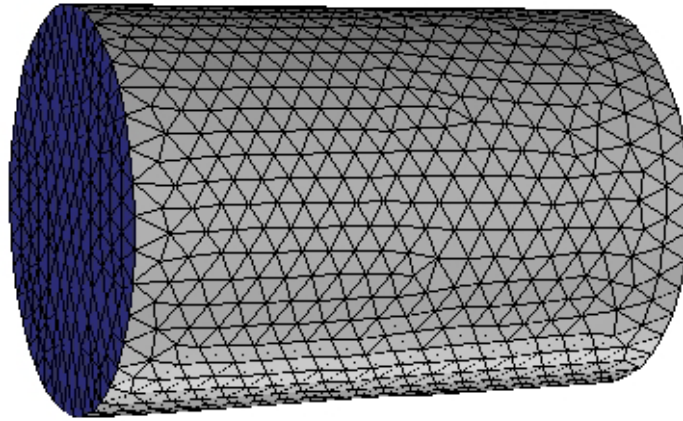
(a) Mesh of whole domain
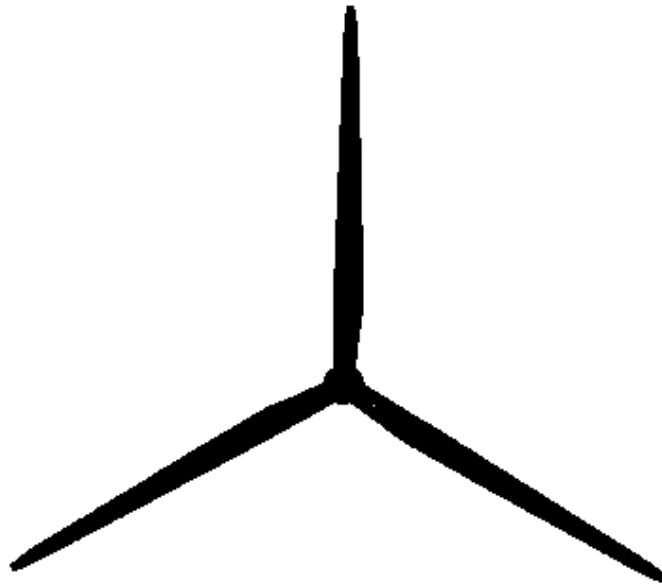
(b) Mesh of the wind turbine blade

Figure 5. Mesh generation

Figure 5 continued
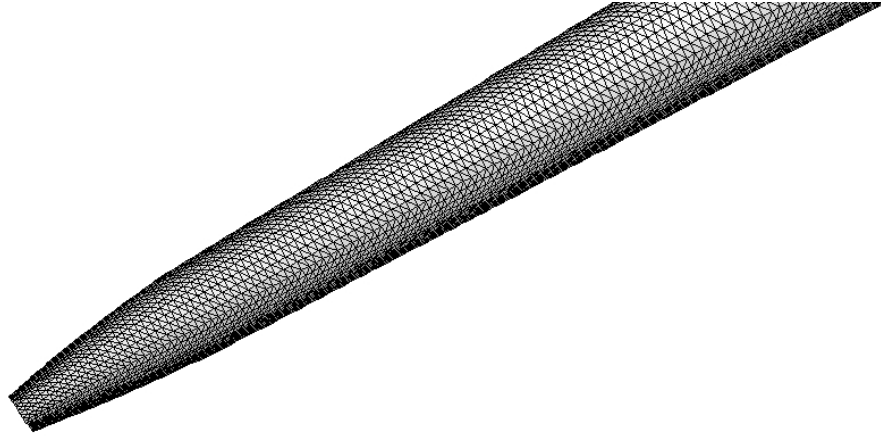
(c) Mesh of the enlarged blade
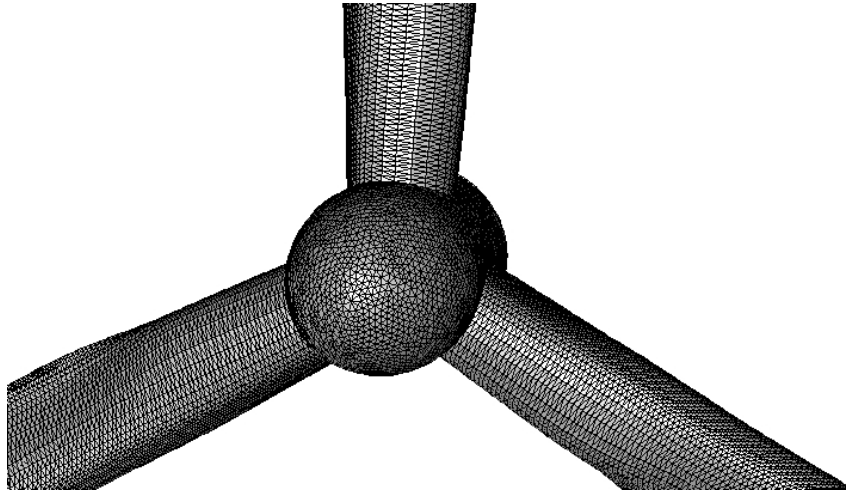
(d) Mesh around the blade hub

Furthermore, mesh independent study is completed as well. It's acknowledged that a finer mesh with more cells could increase simulation accuracy, but it would also add computational workload and prolong simulation time. By contrast, if a coarser mesh is implemented, it would take less time to run the calculation, but the results would also be less accurate. Thus, an appropriate mesh is required to generate for both accuracy and saving the simulation time. Mesh independent study is used to achieve this purpose.

Three different mesh settings are generated for mesh independent study and are demonstrated in Table 2. The coarse mesh has about 1.6 million cells, the medium mesh has nearly

2.4 million cells, and the fine mesh has about 4.3 million cells. As mentioned above, the more cells the mesh contains, the finer the mesh would be. Thus, coarse mesh is the coarsest mesh, and fine mesh is the finest mesh.

Figure 6 is about the pressure coefficient at the location where r/R equals to 0.63 when the inlet wind speed is equal to constant 9 m/s. It is designed to identify whether the results under different mesh conditions are precise enough. t may be displayed that the largest coefficient of pressure from coarse mesh is over 1.5, while the result from fine mesh shows the largest pressure coefficient is only about 1.25. The results from coarse mesh and fine mesh shows evident difference. At the same time, the largest pressure coefficient from medium mesh is nearly 1.30, which is close to the results from fine mesh. Besides, when observing the whole curve of the pressure coefficient, it is not difficult to find that the curve from medium mesh shows high consistency with the finest mesh, fine mesh. As a result, medium mesh is chosen for this paper's simulation based on accuracy and computing time.

Table 2. Mesh statistics

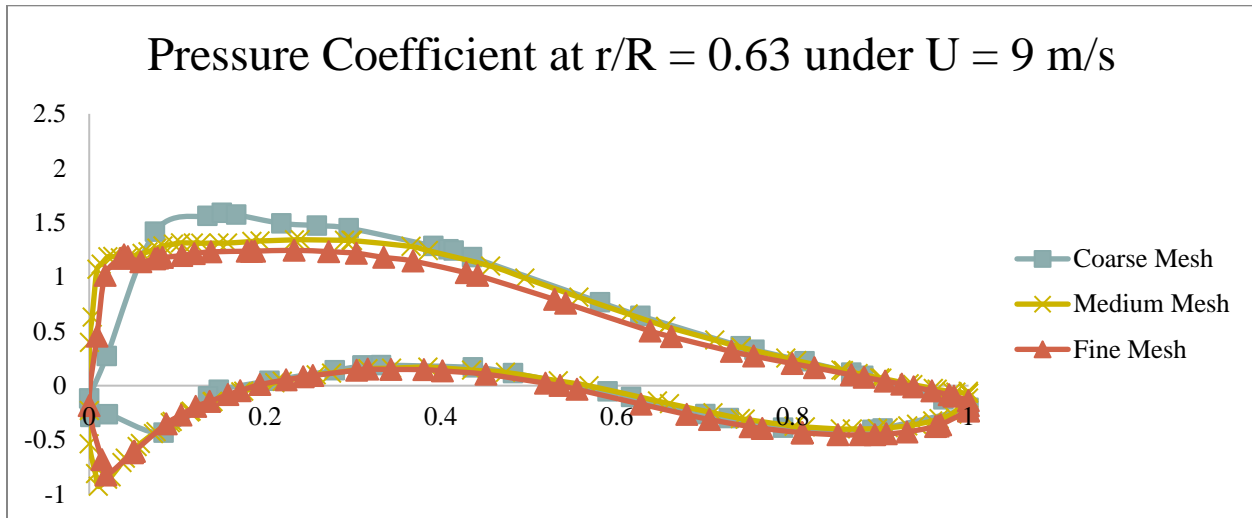| Mesh	Coarse mesh	Medium mesh	Fine mesh
Cells	1,613,463	2,479,240	4,262,617

Figure 6. Pressure Coefficient at r/R = 0.63 under U = 9 m/s

3.3   Computational Domain and Boundary Setting

In order to make sure that simulation results are reasonable, the simulation model for NREL 5-MW offshore wind turbine was initially validated with Zhao's [24] work. Therefore, the computational domain in this paper set the same as his model. Since the floating structure isn't taken into consideration, the CFD simulations are conducted only considering the rotor blades. The center of the rotor blades is coincident to the center of global coordinate. As can be observed in Figure 7, two domains consisting of computational fluid domain and rotating domain are generated. The rotating domain contains the rotor blade as a smaller cylinder of a 62.9 m in radius. While the computational fluid domain has a radius of 200 m. the global coordinate setting is presented in Figure 7 as well. The origin point of the global coordinate is set as the center of the turbine blade, which is also the center of the hub. The side view of two computational domain is shown in Figure 8 as well. Three surfaces are named as inlet, outlet, and wall respectively. The distance from inlet to the rotor blade is 100 m and the length between the rotor blade and the outlet is 250 m.

As for the current calculation, the cell zone conditions, and boundary conditions setting are included in Table 3 and Table 4. The rotating domain is set as the mesh motion with a rotational velocity. Inlet of velocity and outlet of pressure were set as well for the boundary condition.
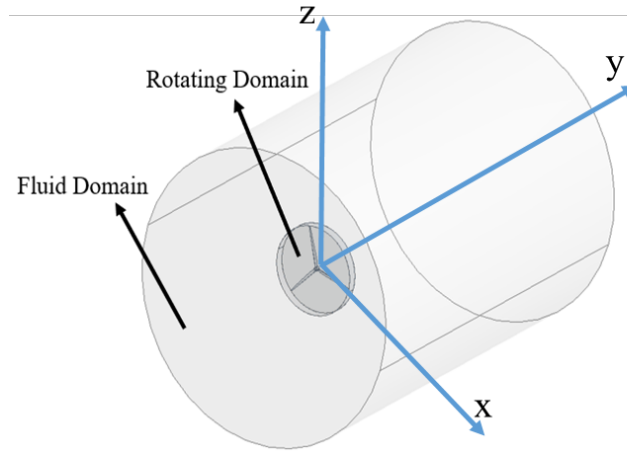
Figure 7. Computational domain
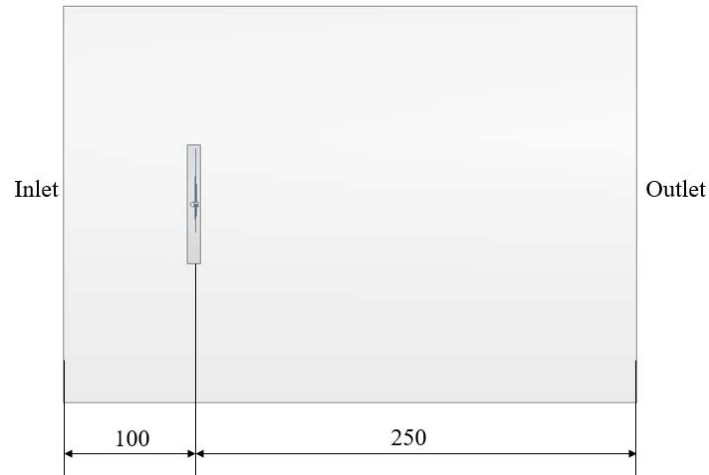
Figure 8. Side View of whole computational domain

Table 3. Cell Zone Conditions

Zone Name	Description
Rotating Domain	Mesh motion, Rotational Velocity
Computational Fluid Domain	Rotation axis

Table 4. Boundary Conditions

Name	Boundary Conditions Description
Inlet	Velocity Inlet, Velocity Magnitude and Direction, K and Epsilon Method
Outlet	Pressure Outlet, Intensity and Viscosity Ratio Method
Turbine Blade (Blade 1, Blade 2, Blade 3 and Hub)	Stationary Wall, Rotational Axis, Speed = 0, Roughness Height = 0
Wall	Moving Wall, No Slip, Roughness Height = 0

3.4   Turbulence Model

Commercial software ANSYS Fluent is selected to run the numerical simulation in this work. It offers access to visualize and deliver the value of simulation. Thanks to the software, the rotating motion and the dynamic performances of the wind turbine can be observed, which is an excessive support to wind turbine analysis.

Compared to the Large Eddy Simulation (LES) model, which is used in Wang's work, RANS model is picked for the current work. The averaged flow is transported using the Reynolds-averaged Navier-Stokes (RANS) equations and full turbulence spectrum id described as well. As a result, the RANS modeling approach greatly decreases the computing burden and resources required. LES offers an alternative method to compute only the smaller eddies by filtering the large eddies through a time-dependent simulation. By reducing turbulence modeling, the errors introduced by turbulence modeling are reduced. Whereas LES methods requires a large amount of computational resources. Taking into account the fact that RANS model provides a relatively accurate simulation results and notable simulation efficiency compared to LES model, RANS model is used for this work.

The velocity field of a flow can be divided into a mean part and a fluctuating part

$$u_i = \overline{u_\iota} + u_i' \tag{13}$$

$$p_i = \overline{p_\iota} + p_i' \tag{14}$$

The continuity equation of the incompressible Navier-Stokes equations is written as

$$\frac{\partial u_i}{\partial x_i} = 0 \tag{15}$$

And the momentum equation is expressed as

$$\rho \left(\frac{\partial u_i}{\partial t} + u_j \frac{\partial u_i}{\partial x_j} \right) = -\frac{\partial p}{\partial x_i} + \mu \left(\frac{\partial^2 u_i}{\partial x_j \partial x_j} \right) \tag{16}$$

Substituting equation (16) with equation (13) and (14), and after apply averaging, the RANS equation is described as

$$\rho \left(\frac{\partial \overline{u_\iota}}{\partial t} + \overline{u_\jmath} \frac{\partial \overline{u_\iota}}{\partial x_j} \right) = -\frac{\partial p}{\partial x_i} + \frac{\partial}{\partial x_j} \left(\mu \frac{\partial \overline{u_\iota}}{\partial x_j} - \rho \overline{u_i' u_j'} \right) \tag{17}$$

Turbulence models consists of standard, RNG, and realizable k-ε models. The main differences in the models are the ways to estimate the turbulent viscosity. The standard k- ε model,

which is a two-equation model, is the most basic model of turbulence. The turbulent velocity and length scales may be estimated separately with the use of two equation solutions. While, RNG k-ε model is identical to the standard one. The difference is that RNG model has an extra term in its ε formula that increases the precision for quickly strained flows. As for realizable k- ε model, it is a comparatively new enhancement. A novel formula for the turbulent viscosity is included. Realizable means that the model fulfills specific mathematical limitations in terms of Reynolds stresses, which are compatible with turbulent flow physics. In addition, it is effective for rotational flow simulation. And it is defined as

$$\frac{\partial}{\partial t}(\rho k) + \frac{\partial}{\partial x_j}(\rho k u_j) = \frac{\partial}{\partial x_j}\left[\left(\mu + \frac{\mu_t}{\sigma_k}\right)\frac{\partial k}{\partial x_j}\right] + G_k + G_b - \rho\varepsilon - Y_M + S_k \qquad (18)$$

and

$$\frac{\partial}{\partial t}(\rho\varepsilon) + \frac{\partial}{\partial x_j}(\rho\varepsilon u_j) = \frac{\partial}{\partial x_j}\left[\left(\mu + \frac{\mu_t}{\sigma_\varepsilon}\right)\frac{\partial\varepsilon}{\partial x_j}\right] + \rho C_1 S\varepsilon - \rho C_2 \frac{\varepsilon^2}{k + \sqrt{\nu\varepsilon}} + C_{1\varepsilon}\frac{\varepsilon}{k}C_{3\varepsilon}G_b + S_\varepsilon \quad (19)$$

where

$$C_1 = max\left[0.43, \frac{\eta}{\eta + 5}\right], \eta = S\frac{k}{\varepsilon}, S = \sqrt{2S_{ij}S_{ij}} \qquad (20)$$

4. RESULTS AND DISCUSSION

In this paper, the aerodynamic performances of NREL offshore 5-MW wind turbine under different fixed wind speeds in the range of 3m/s to 25m/s are simulated. The rotor torque, thrust, power, power coefficient, pressure coefficient, wake vortices and velocity profiles are obtained in detail. 8 cases are designed and listed as Table 5. Case 1, 2, 3 and 4 are under the rated wind speed (11.4 m/s), and case 5 is at 11.4 m/s. While case 6, 7 and 8 are over the rated wind speed. First and foremost, Case 4 is validated by comparing the rotor torque and efficiency to numerical results from reference paper, and reasonable agreement is found. Then, further simulations are run to obtain the aerodynamic features. The aerodynamic features from various cases are also compared with each other. The simulated cases are presented in Table 5.

Table 5. Simulation Cases

Case	Inlet wind velocity (m/s)	Rotation speed (rpm)
1	4.00	7.18
2	5.00	7.39
3	8.00	9.16
4	9.00	10.30
5	11.40	11.89
6	15.00	12.10
7	20.00	12.10
8	25.00	12.10

4.1 Model Validation Study

Validation was done for Case 4, when the wind velocity inlet U was equal to uniformly 9 m/s. The simulated torque was compared with others' work. In Zhao's work, the final torque was 2682 kNm, and it was employed to compute the power, the answers turned out to be 2.89 MW. Besides Zhao's [24] work, the simulated torque was also compared with Jonkman's [17] numerical

results. The absolute value of torque from Jonkman's work was 2474.5 kNm and the generated power was 2.67 MW.

Table 6 demonstrates the simulated torque for Case 4. The time averaged absolute value of the torque is equal to 2596.96 kNm. Each blade donated nearly 1/3 of the torque to the total value.

Table 6. Torque distribution

Part	Torque (kNm)
Blade 1	-866.89
Blade 2	-864.12
Blade 3	-865.94
Hub	0.35
Total	-2596.96

The power generated can be determined using

$$P_0 = T_{f0} \times \omega = 2596.96\,kNm \times 1.079\,rad/s = 2.80\,MW$$

The error of the torque and power generated can be calculated using

$$\frac{2596.96 - 2474.5}{2474.5} \times 100\% = 4.94\%$$

Table 7 states the torque from different reference paper, and the errors with their work are calculated and presented. From Table 7, it is observed that the error between simulated torque and Zhao's [24] work is the lower than the error with Jonkman's [17] results. However, the error from Jonkman's work is quite close to the error from Zhao's result. Moreover, the error calculates from Jonkman and Zhao are as low as enough to validate the current setting, in consideration of the fact that errors are even not over 5%. Thus, the current setting and mesh is identified as feasible for the after simulation analysis.

Table 7. Torque comparison

Simulated torque: 2596.96 kNm		
	Torque (kNm)	Error (%)
Zhao	2682.00	3.17
Jonkman	2474.50	4.94

Compared the simulated torque with that from the reference, good agreement is observed. Consequently, the current numerical model and the setting is appropriate for the following cases study.

4.2 Inflow Condition Effects on Flow Around Wind Turbine Blades

Three different wind inflow profiles based on case 4 are illustrated in Figure 9. The first condition is the uniform velocity inlet condition. The inlet wind speed remains the same along the z axis as has been shown. The second condition is power law velocity inlet. The wind profile power law is described as

$$u(z) = u_{ref} \left(\frac{z}{z_{ref}} \right)^{\alpha} \tag{21}$$

Where $u(z)$ refers to the wind velocity at certain height z, u_{ref} represents the hub velocity, which would be consistent with the uniform inflow velocity, 9m/s. z_{ref} is the height of the hub. In this study, the exponent α is selected as 0.35 [27]. Considering the global coordinate setting, the wind profile power law in this study is expressed as

$$u(z) = 9 \left(\frac{z + 225}{225} \right)^{0.35} \tag{22}$$

The last condition is linear approximation velocity inlet. When the height of the hub is equal to zero, the velocity of the hub is 9 m/s. Then linear approximation can be described as
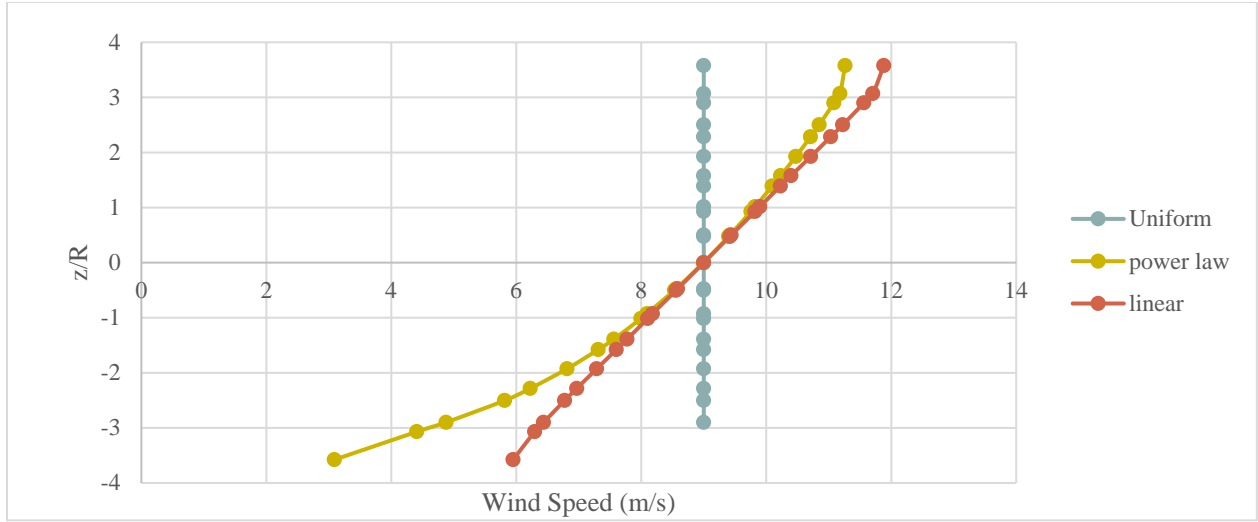
$$u(z) = 0.014z + 9 \tag{23}$$

Figure 9. Wind inflow conditions

Figure 10 demonstrates the distribution of velocity at various plane under three different inflow conditions. The contour on the left side is at x = 0 plane, the contour in the middle is at y/R = 1 plane, and the figure on the right is the enlarged region from y/R = 1 plane. In uniform velocity case, it is obvious that the velocity of the region in front of the blade is equal to 9 m/s evenly because the color on the contour distributes evenly. The inflow velocity slows down after going through the turbine. The velocity contours of linear approximation case and power law case shows higher similarity except at the bottom of the computational domain. It is observed that the bottom of the computational domain from linear velocity inlet is smaller than the same part from power law velocity inlet. It can be explained through Figure 9. When z/R is smaller than -2, the corresponding wind speed from linear case in smaller than power laws. The results of the velocity contours under different inflow conditions shows reasonable agreement with Zhou's work [27]. The upper part of the computational domain contains higher velocity than the lower part. The results turn out to be consistent with Figure 9. While the velocity behind the rotating blade is almost the same with constant inlet. This may be explained by the velocity of the hub is the same.

The enlarged contour shows the low velocity region. In the uniform velocity case, the low velocity region is like a ring shape and is shows the symmetric structure. But in both linear and power law case, the low velocity region shows few differences. The low velocity regions in both cases are like crescent shapes and they are no longer symmetrically. The low velocity region shifts to the right direction a little bit. This may be explained by that the wind turbine is rotating in a
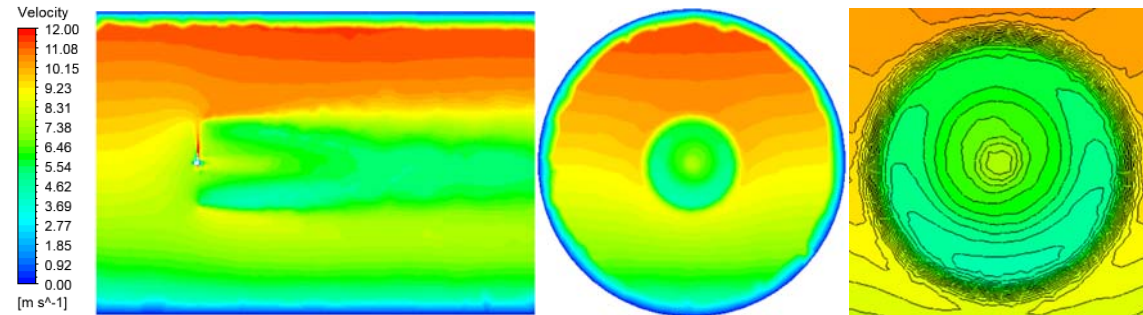
counterclockwise direction. The rotating wake transports the momentum from the high wind to the low wind (left side) and from low wind to high wind (right).
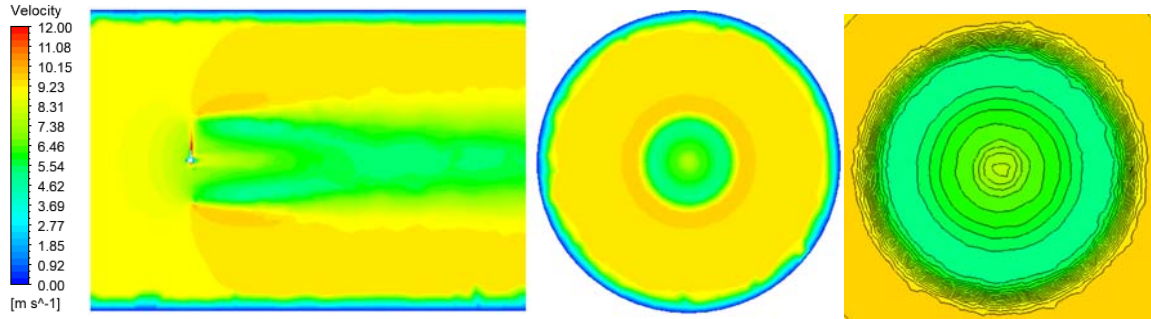
(a) Uniform velocity inlet
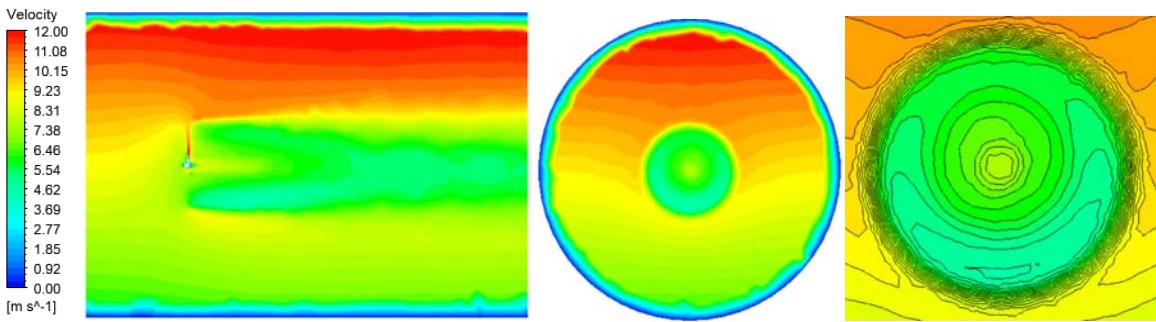
(b) Linear velocity inlet

(c) Power law velocity inlet

Figure 10. Distribution of velocity under different inflow conditions

4.3 Wake Vortex Development

Figure 11 presents the iso-surfaces of $Q = 0.008$ under different velocity inlet, and it clearly demonstrates the wake vortices near and behind the blades. The wake vortex is one of the most significant properties for the aerodynamic analysis of the turbine blade. Especially the wake

vortices around the turbine blades have massive impact on their aerodynamic properties. Additionally, Q is a second invariant velocity gradient tensor. It is used to capture the wake vortices around the blades and indicates the wake vortices. Q is expressed as

$$Q = \frac{1}{2}\left(\Omega_{ij} \times \Omega_{ij} - S_{ij}S_{ij}\right) \tag{24}$$

Where Ω_{ij} represents the vorticity tensor and S_{ij} represents the rate of strain tensor.

The wake patterns at the back of the wind turbine rotor under different wind speed are visualized in Figure 11. Since the wind turbine blades are rotating, the turbine blades and the surrounding fluid would interact with each other. The vortices are generated thank to the interaction. The vortices perform helically, intensely, and symmetrically and then dissipate. With the increase of wind speed, the helical vortices could persist in a longer downstream distance. The tendency of the helical path with the increasing wind speed presents reasonable consistency with Zhao's work [24].
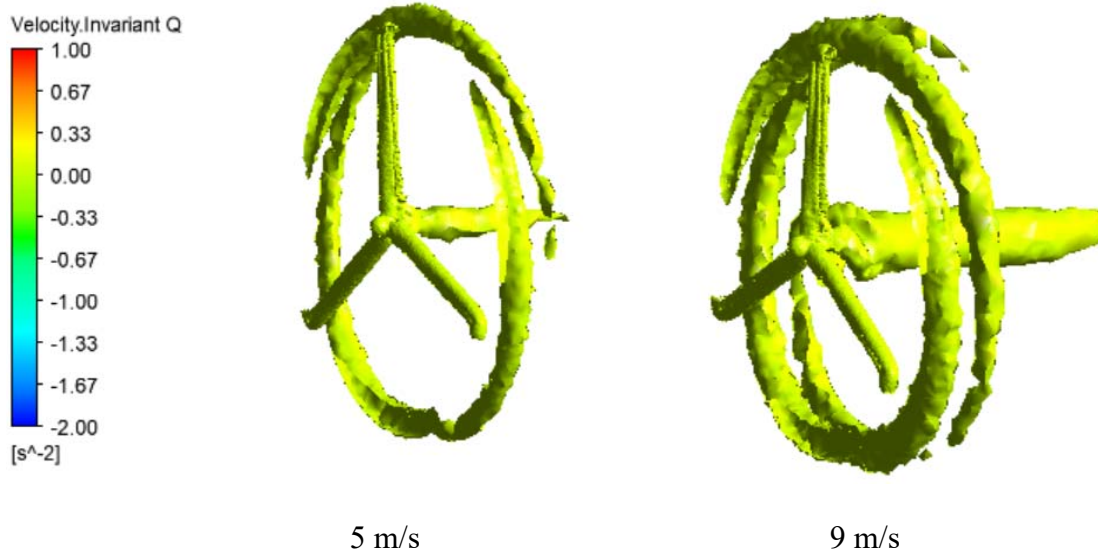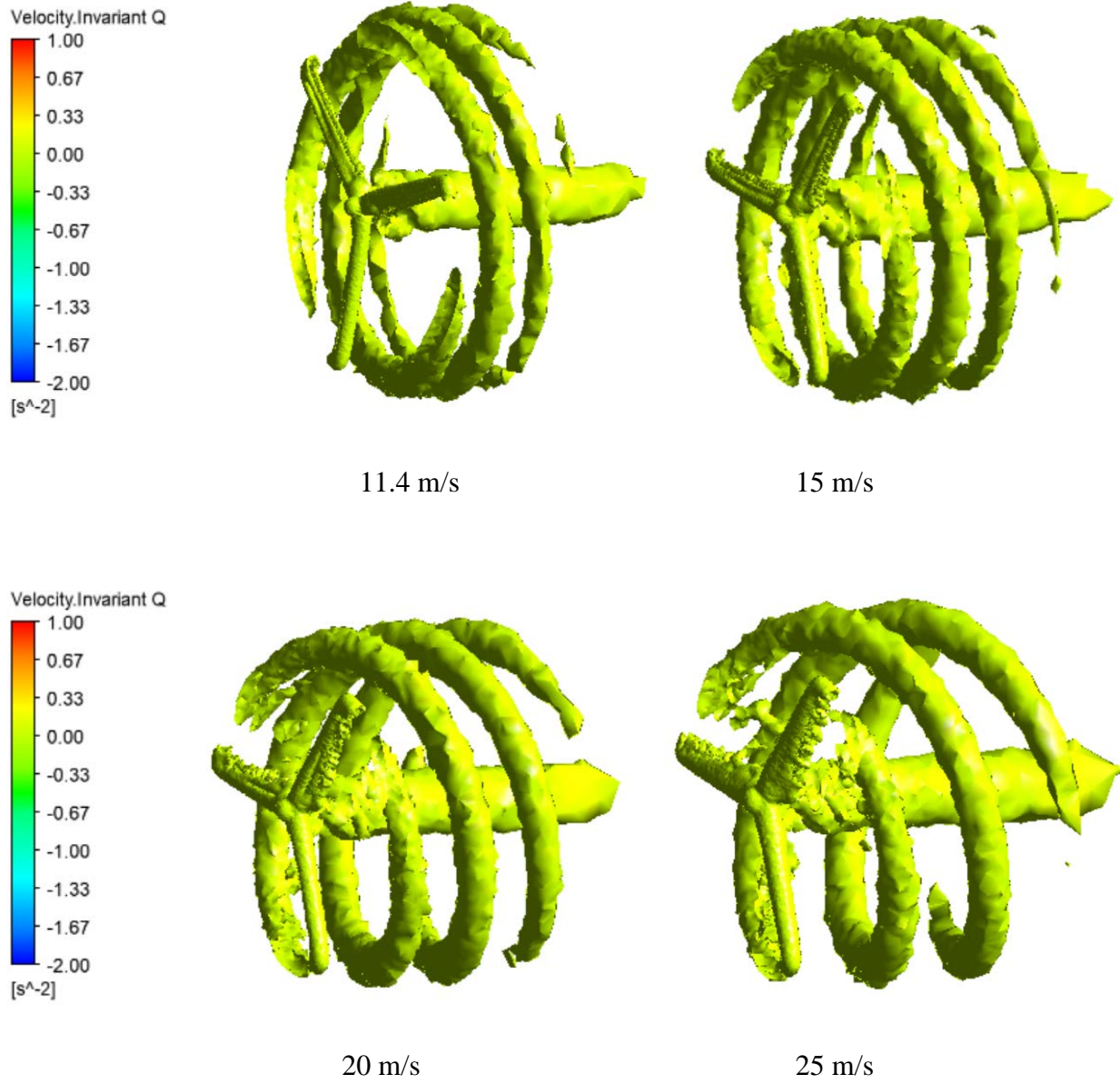

5 m/s   9 m/s

Figure 11. Iso-surfaces of Q = 0.008 under U = 5, 9, 11.4, 15, 20, 25 m/s

Figure 11 continued

11.4 m/s   15 m/s

20 m/s   25 m/s

4.4   Near Wake Flow Features

6 selected locations are shown in Figure 12. The locations are in the direction of downriver of the wind turbine. The selected locations are y/R = 1, y/R = 2, y/R = 3, y/R = 4, y/R = 5, y/R = 6 respectively.
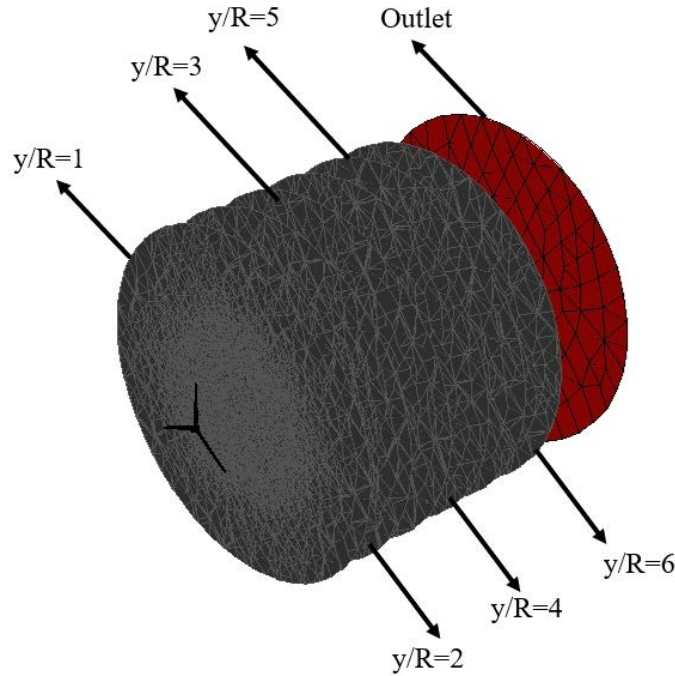
Figure 12. Selected Locations

The velocity profile at various selected locations under different wind speed are demonstrated in Figure 13. y/R indicates the vertical position, u is local wind velocity and U is wind speed. First and foremost, when the inlet velocity remains the same, the velocity deficit reaches the peak at y/R = 1 location, which is the nearest location to the wind turbine blade. With the y/R increases, which means the selected locations gradually move away from the wind turbine, the velocity deficit decreases. What's more, the center of the velocity profile may be influenced by the wind turbine hub. Focusing on the location y/R = 1,2 and 3, it can be observed that the velocity variation around the center is enormous. When the selected location is nearly to the turbine hub, the influence to the velocity profile is great. Putting emphasis on the location y/R = 4, 5 and 6, it is easy to find that the velocity barely changes. Thus, when the selected location is gradually far away from the hub, the influence of the wind turbine hub decreases. The velocity recovery process is vividly presented. Somewhere after a downstream of 4r, there is an apparent change from double-Gaussian to single-Gaussian distribution.

Compared the velocity profiles under different wind speed, it can be concluded that as the inlet wind speed keep increasing, the influence of the hub on velocity profile reduces. Especially when observing the velocity profile at y/R =1 location under different wind speed, the velocity

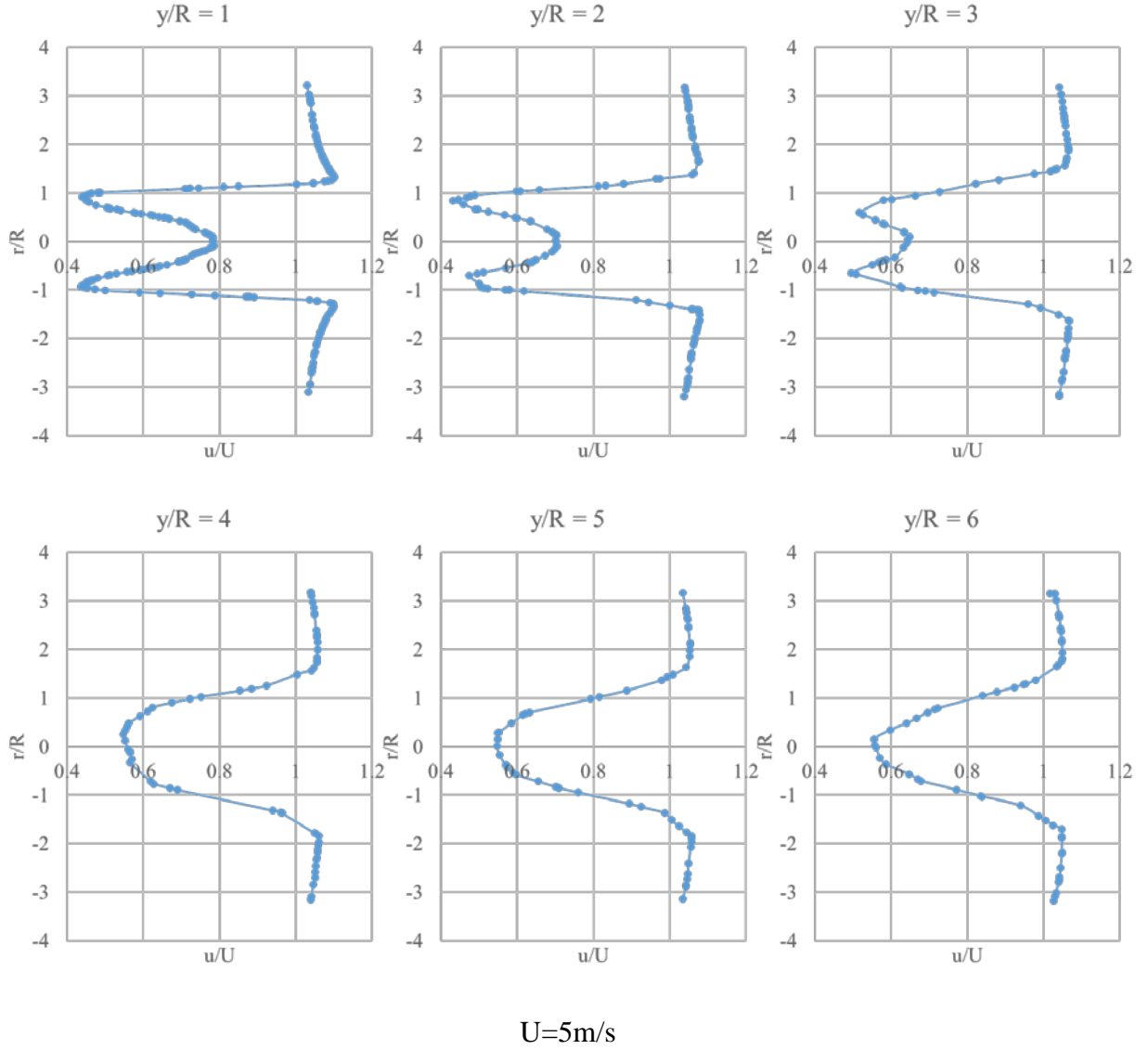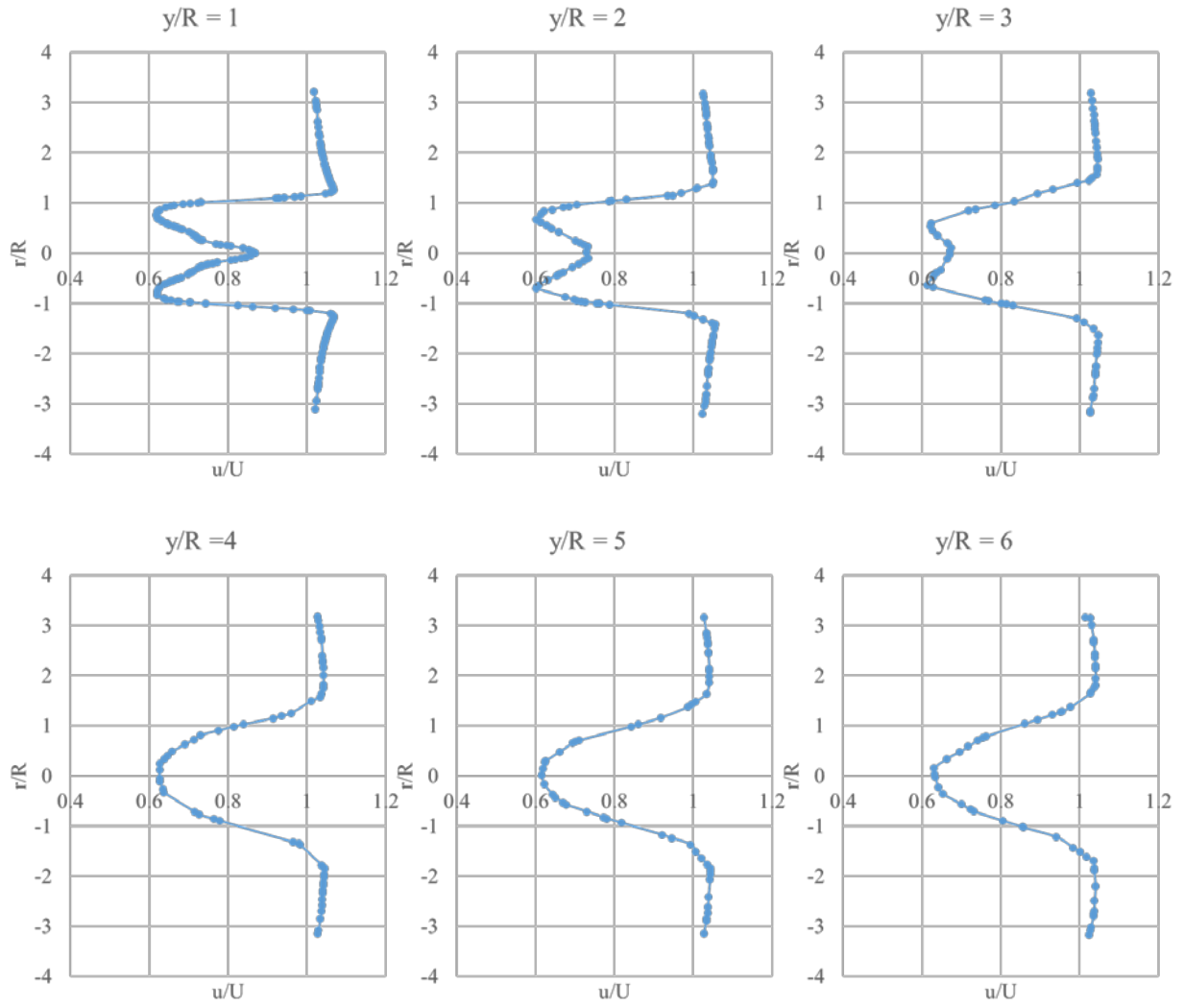variation around the center when u = 5 m/s is massive compared to the velocity variation under u = 25 m/s.

U=5m/s

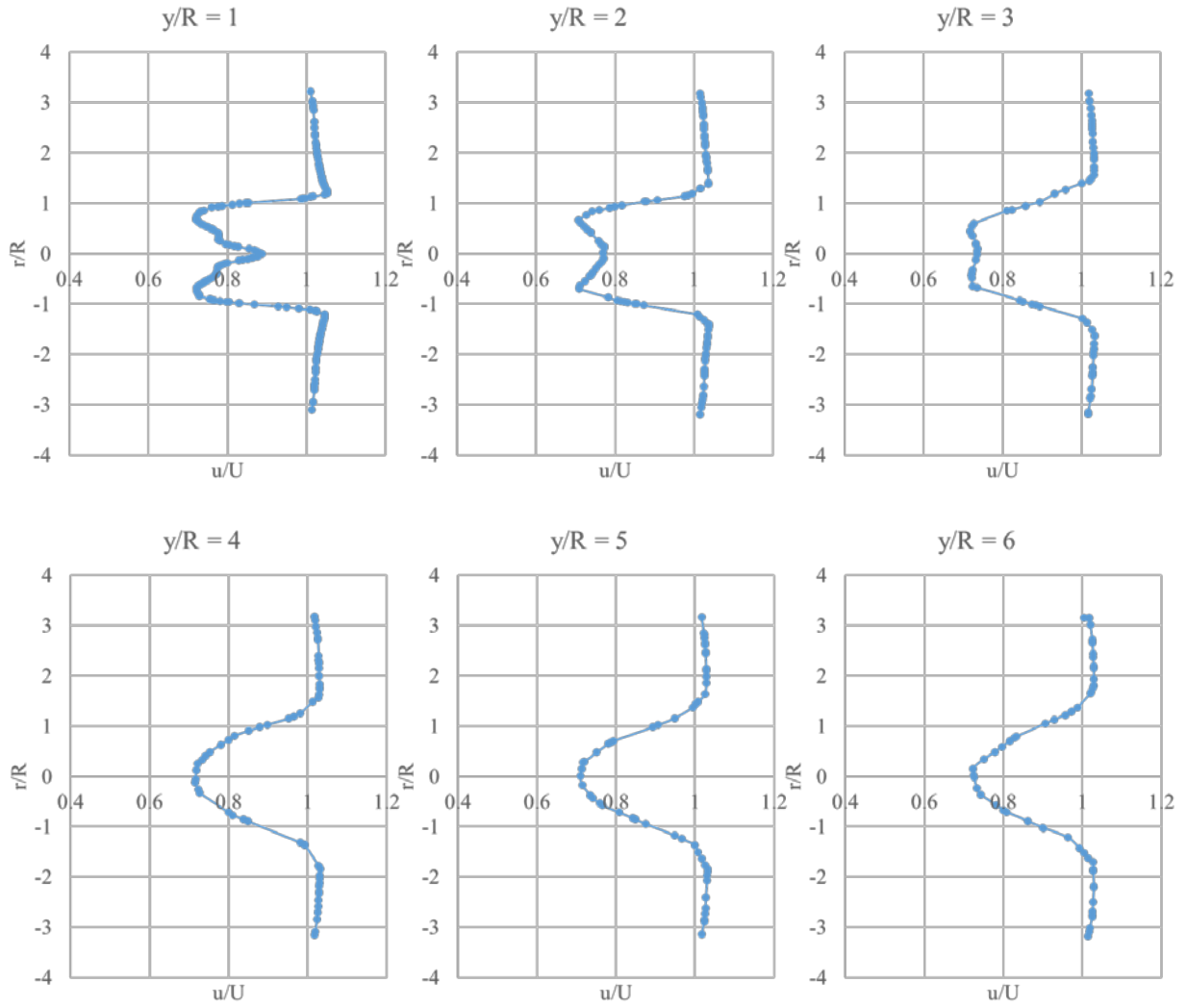Figure 13. Velocity profile at y/R = 1,2,3,4,5,6 under U=5, 11.4, 15, 20, 25 m/s
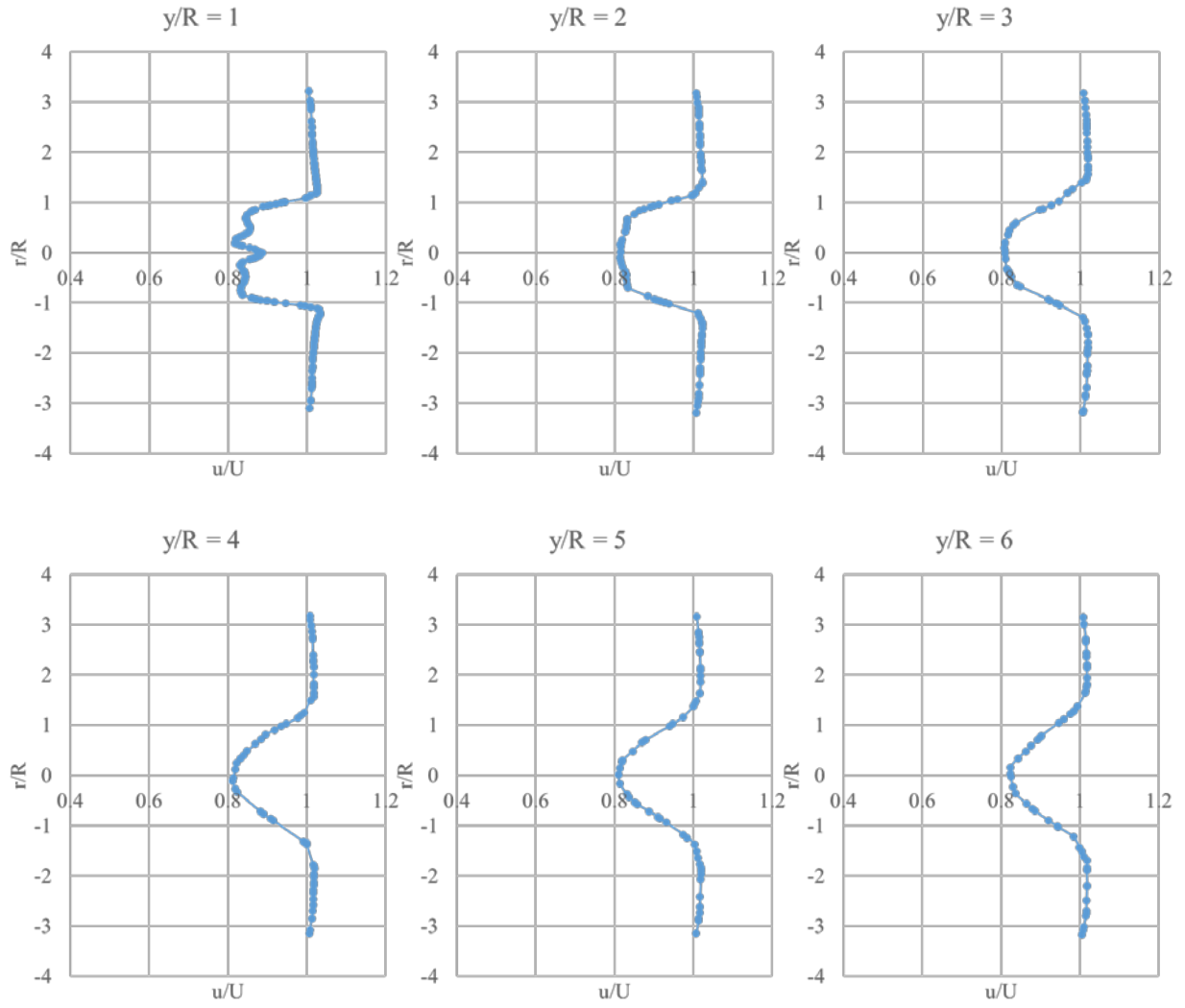
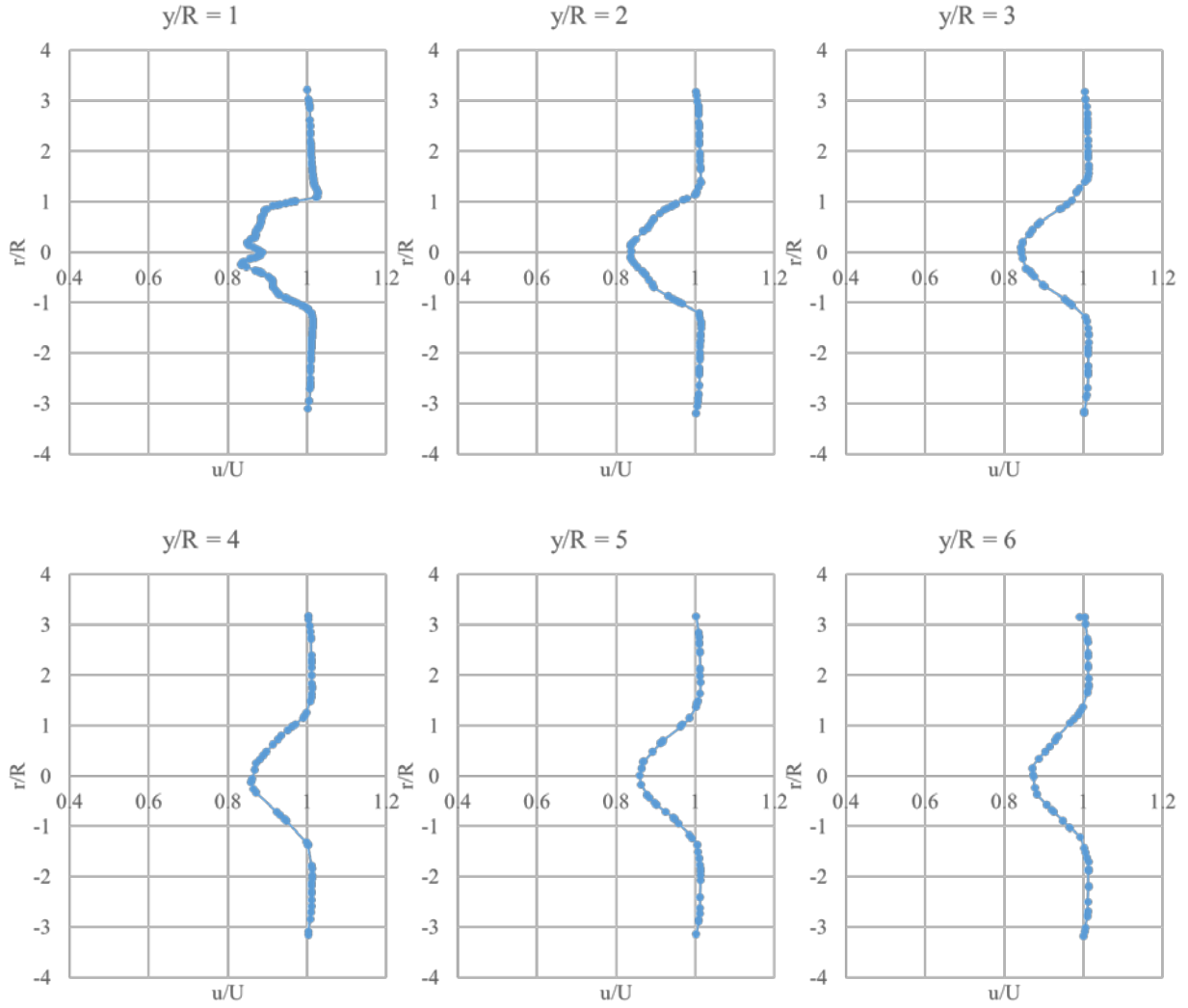Figure 13 continued

U=11.4 m/s

Figure 13 continued

U=15 m/s

Figure 13 continued

U = 20 m/S

Figure 13 continued

y/R = 1   y/R = 2   y/R = 3

y/R = 4   y/R = 5   y/R = 6

U = 25 m/s

4.5   Wind Flow Features near Turbine Blades

Since the near blade flow behavior plays a significant role on the rotor, the flow near the blade needs to be discussed. Limiting streamline offers a method to exhibit detailed flow structure. Limiting streamline is a streamline whose distance normal to the body surface is tend to zero but not equal to zero and it clearly shows the flow separation.

The limiting streamline along with the distribution od pressure on the suction and pressure side for various conditions are displayed in Figure 14 and Figure 15. The change of limiting streamline on the suction side is evident. It is obvious that flow separation occurs near the root and

leading edge part of the blade. It might be produced by the pressure difference between the blade's leading and following edges. Observing the following five conditions, it is easily to conclude that the near root flow separation seems to extend throughout the majority of the turbine blade as the wind velocity rises. The phenomenon may be generated by rotational centrifugal acceleration. When the inflow wind velocity is large, vortices appear at the trailing edge. The streamline on the pressure side shows little change with the various wind speed. What's more, because of the flow separation in stalled region, the pressure difference between the pressure and suction sides of the root is less, leads to a small lift here.
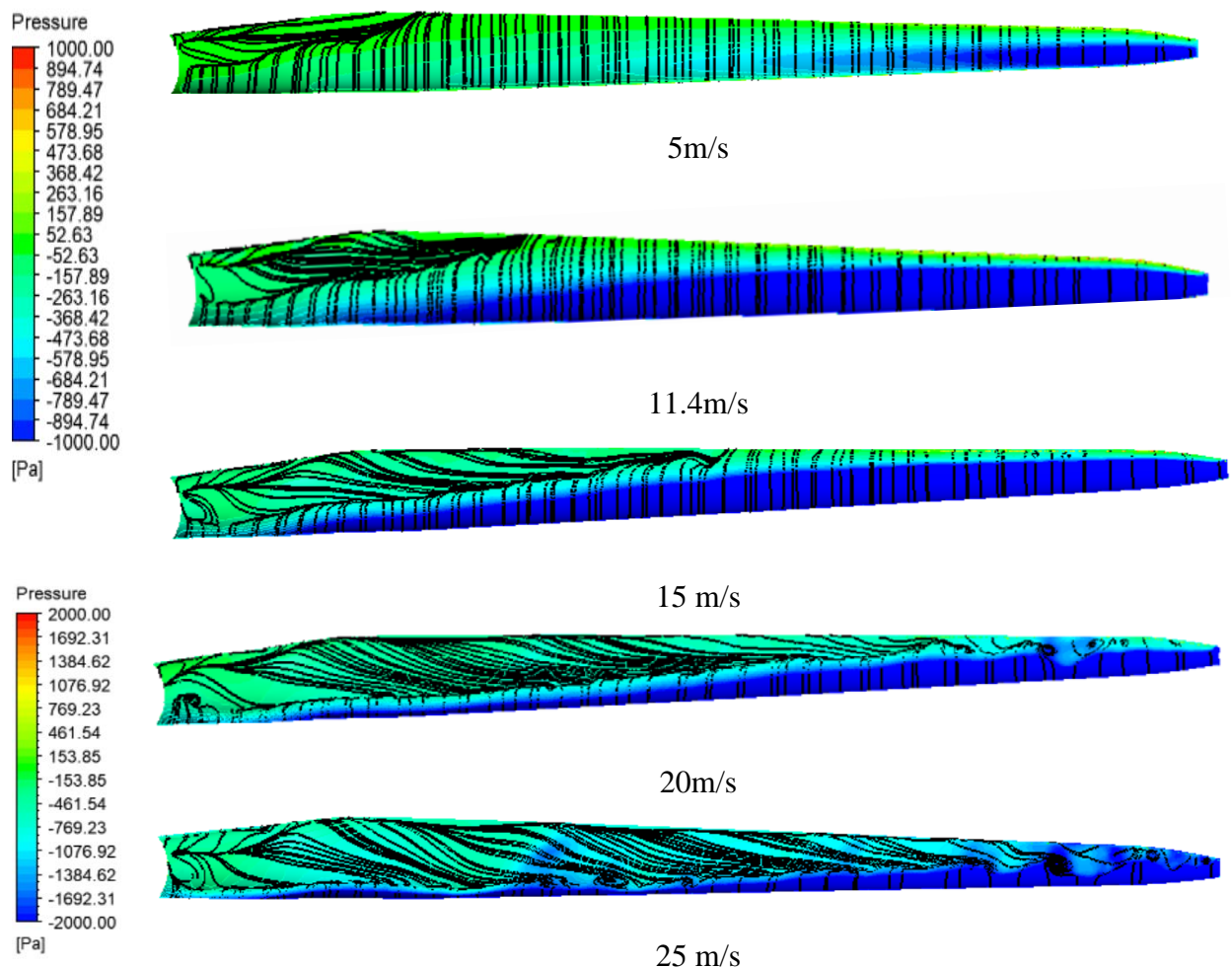

Figure 14. Limiting streamline on the suction side

Pressure
```
1000.00
894.74
789.47
684.21
578.95
473.68
368.42
263.16
157.89
52.63
-52.63
-157.89
-263.16
-368.42
-473.68
-578.95
-684.21
-789.47
-894.74
-1000.00
[Pa]
```

5 m/s

11.4 m/s

15 m/s

Pressure
```
2000.00
1692.31
1384.62
1076.92
769.23
461.54
153.85
-153.85
-461.54
-769.23
-1076.92
-1384.62
-1692.31
-2000.00
[Pa]
```
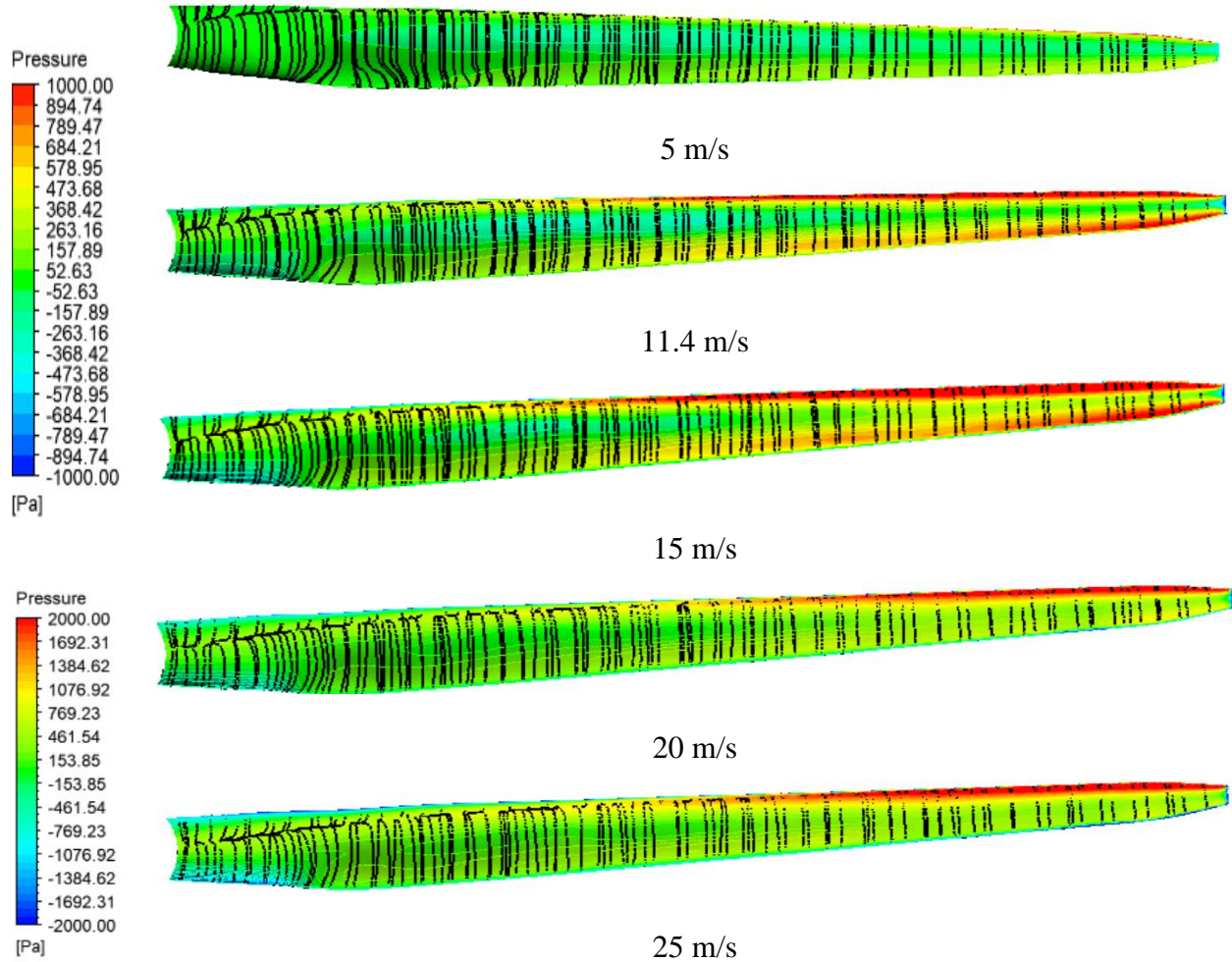
20 m/s

25 m/s

Figure 15. Limiting streamline on the pressure side

4.6   Pressure Analysis

4.6.1   Pressure distribution

Figure 16 presents the pressure distribution all along the blade at r/R = 0.3, 0.63 and 0.95 under various inlet wind speed. r/R represents the different cross section of the turbine blade. It can be observed that the shape of the airfoil at various location is different, which can be explained by those different types of airfoil were located at the selected locations. When r/R = 0.3, Du 35 is implemented for the blade. When r/R is 0.63, Du 21 is used. When r/R = 0.95, NACA 64 is utilized. NACA 64 is more elliptical than the other two selected airfoils.

Apparently, the pressure is increasing as r/R increases, which means the pressure increases from the area near the root to the tip of the blade. In addition, the pressure at both windward side

and suction side increases with the inlet wind speed increases. Especially when the inlet wind velocity is equal to 25 m/s, and the location is at r/R = 0.95, almost at the tip of the blade, the pressure around the airfoil is extremely large. What's more, the pressure on the upper surface is positive, while the lower surface's pressure is negative, indicating that the lift points up.
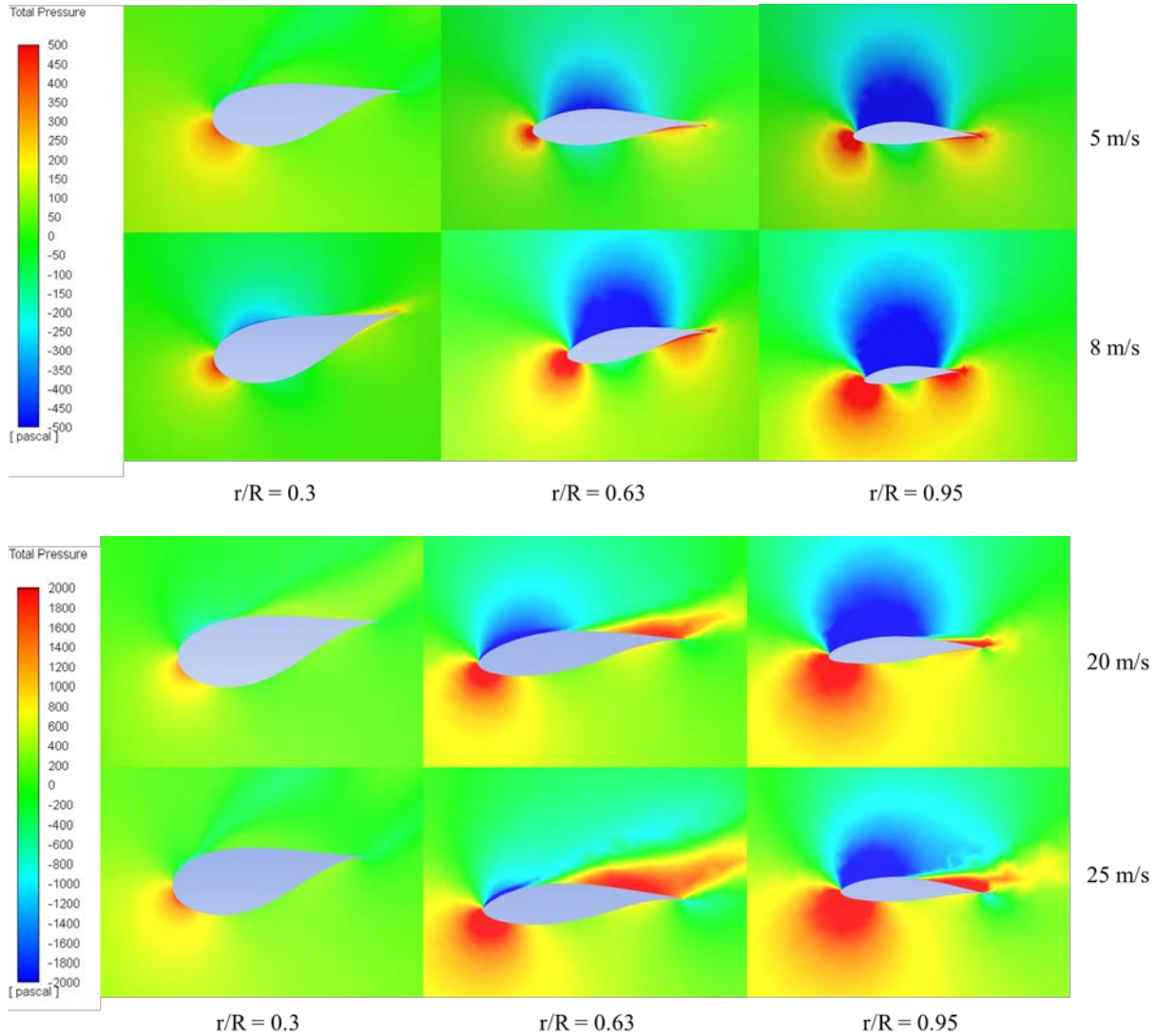

Figure 16. Pressure distribution at r/R = 0.3, 0.63, 0.95 under U = 5, 8, 20, 25 m/s

4.6.2 Pressure coefficient

The pressure at different cross sections along the blade can be obtained from the simulated results. Using the equation below, the pressure coefficient is obtained.

$$C_p = \frac{2(P_0 - P_\infty)}{\rho(U^2 + (\omega r)^2)} \qquad (25)$$

Table 8 and Figure 17 to Figure 21 indicate the consistency with simulated results and reference data. Table 8 shows the error of maximum pressure coefficient under different wind speed inlet at various locations. It indicates that the error of maximum pressure coefficient under U = 8 m/s is the smallest, whereas U = 20 m/s contributes the highest error. When focusing on the locations, it is easily to find that the location where r/R = 0.3 donates the smallest error. The error performances of the rest two planes are almost the same. All in all, the overall average error is roughly equal to 25%.

Table 8. Error of maximum pressure coefficient

Location U(m/s)	0.3	0.63	0.95	Average Error (%)
5	0.92	3.04	25.02	9.66
8	2.86	7.88	10.60	7.11
15	13.74	67.05	34.73	38.05
20	3.01	63.44	55.62	40.69
25	22.63	23.39	42.33	29.45
Average Error (%)	8.63	32.96	33.66	25.08

The pressure coefficient distribution of the selected airfoils, DU 35, DU 21, and NACA 64 under different wind speed inlet is shown in Figure 17 - Figure 21 respectively. From the figures, the simulated pressure coefficient shows great consistency with the reference especially when the wind speed is low. It could be concluded that the leading edge of the airfoil contains more curvature than the trailing edge of the airfoil. The larger inlet velocity leads to a more evident curvature of the leading edge. The differences of pressure coefficient on the leading edge are much larger than the trailing edge, which indicates that the lift is mainly generated from the leading edge.

In addition, it can be concluded that the pressure coefficient at the same selected location shows an increased tendency as the wind speed increases. For case 1, when r/R is 0.3, the largest pressure coefficient is around 2, but for case 8, the largest pressure coefficient is nearly equal to 4

when r/R is also 0.3. Under the condition, the pressure coefficient of case 8 is almost twice as large as case 2.

What's more, the difference of pressure coefficient increases from the root part of the blade to the tip part of the blade. This can be concluded by the fact that the pressure coefficient at r/R = 0.3 is greater than that at r/R = 0.63, not to mention the pressure coefficient at the selected plane r/R = 0.95.
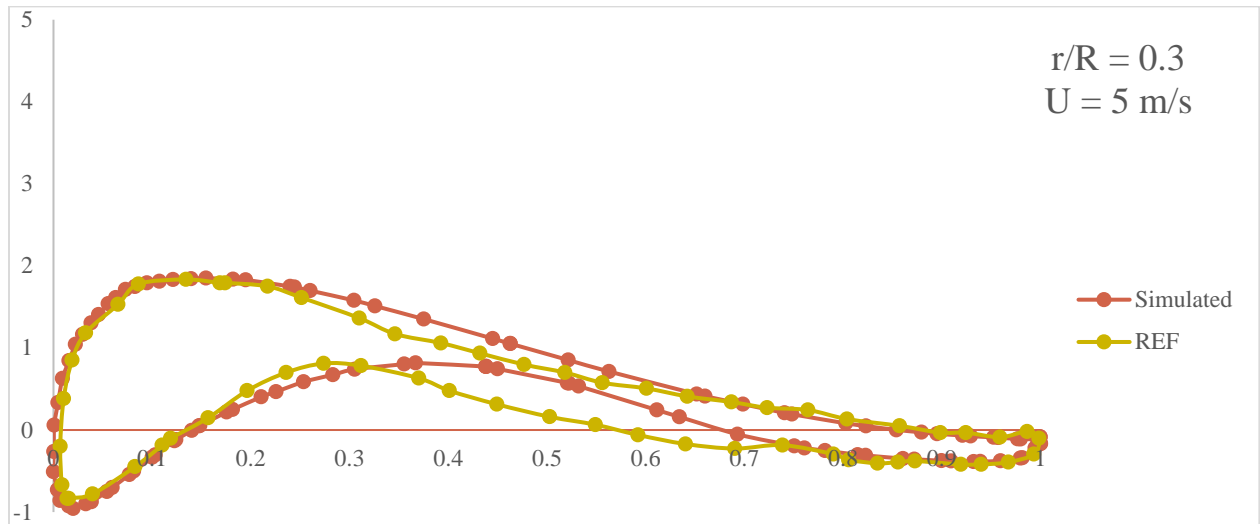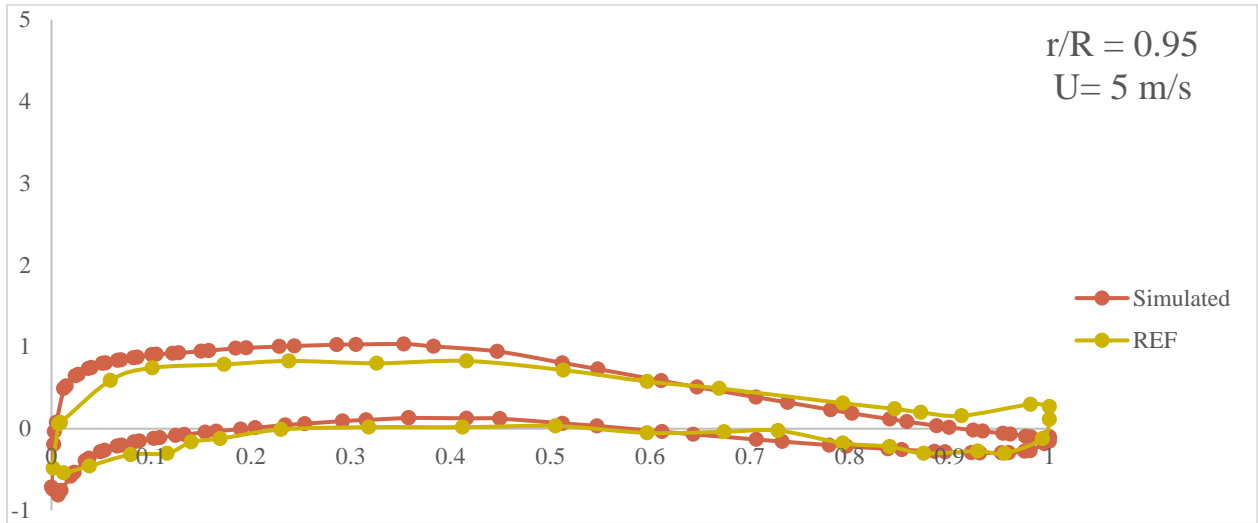
(a)
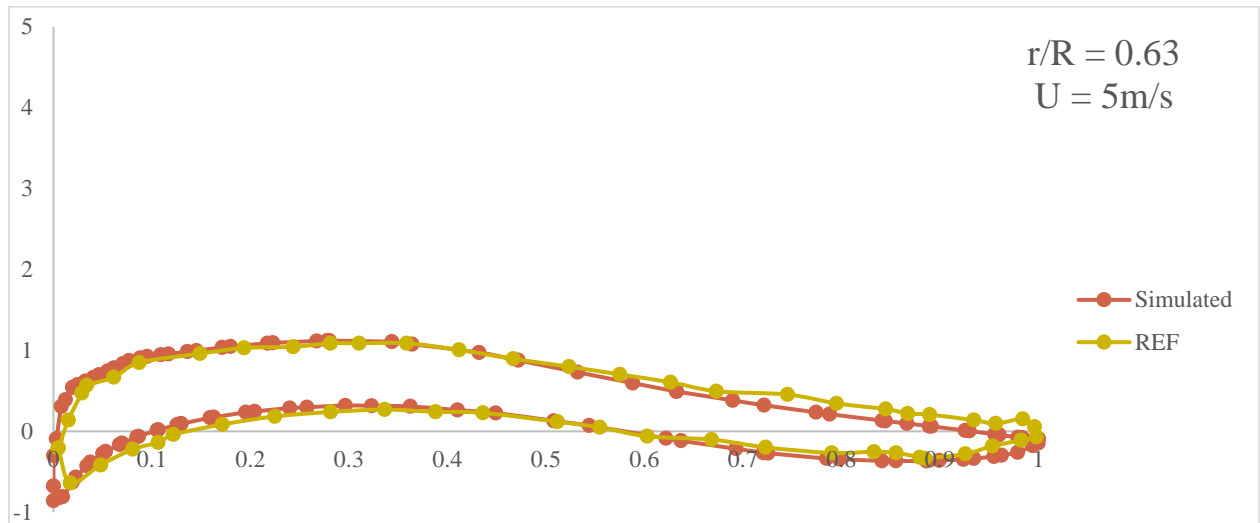
(b)

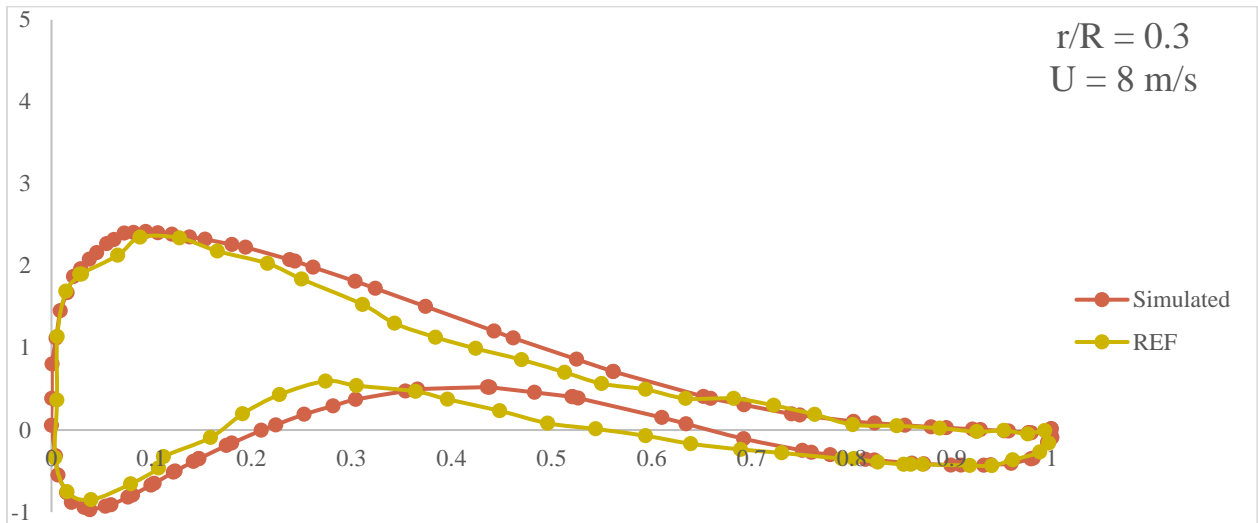Figure 17. Pressure coefficient under U = 5 m/s

Figure 17 continued

(c)
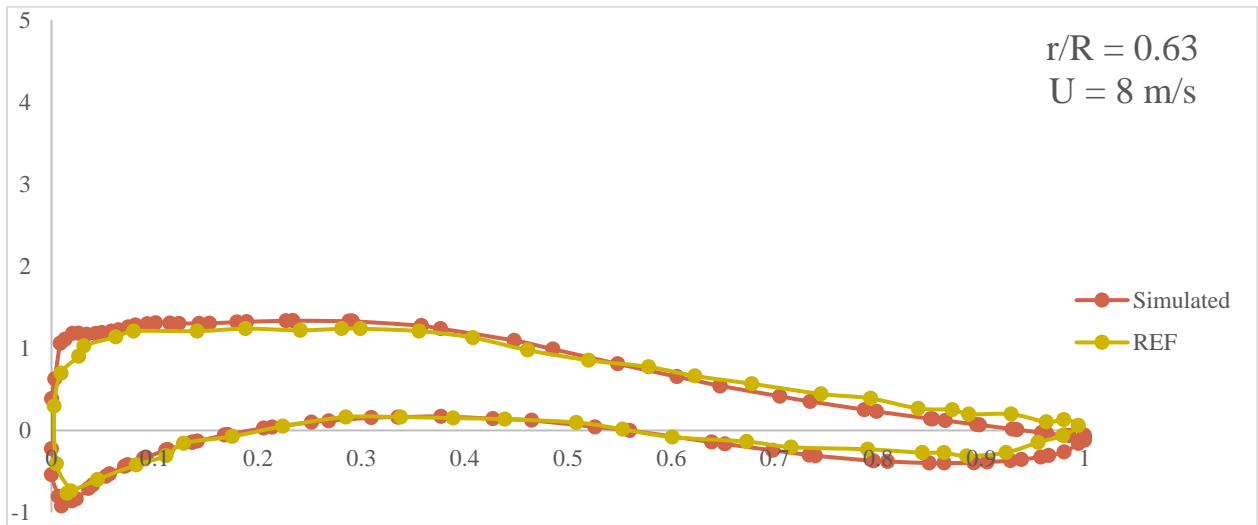

(a)
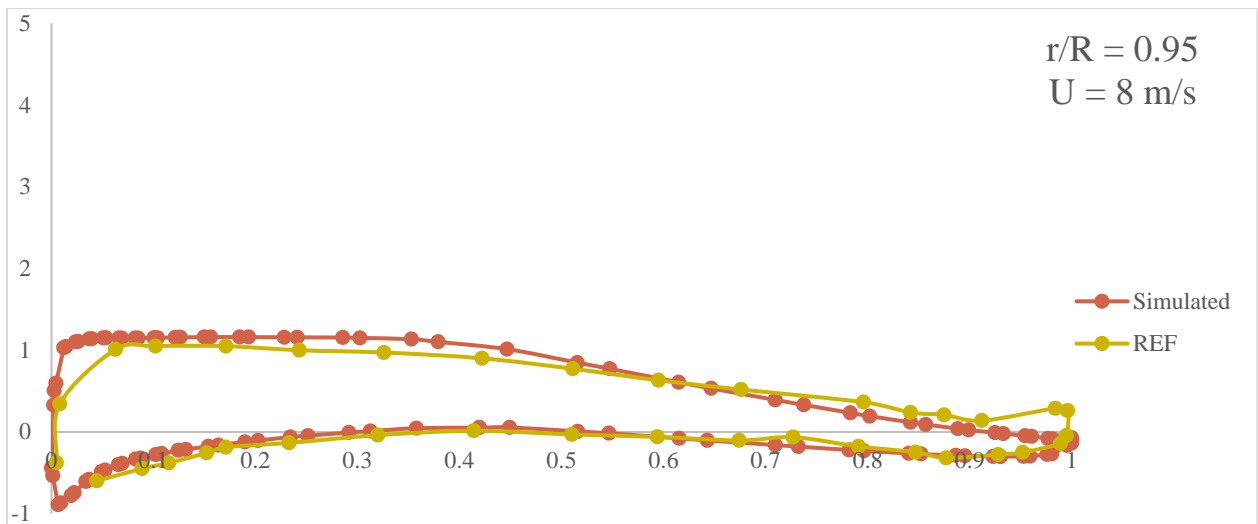
Figure 18. Pressure coefficient under U = 8 m/s

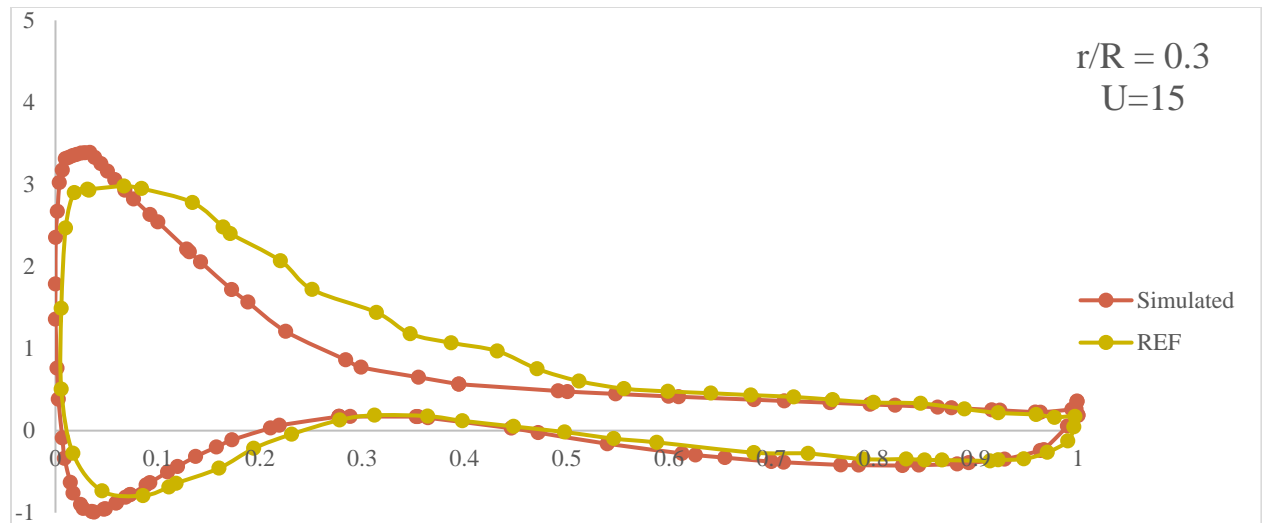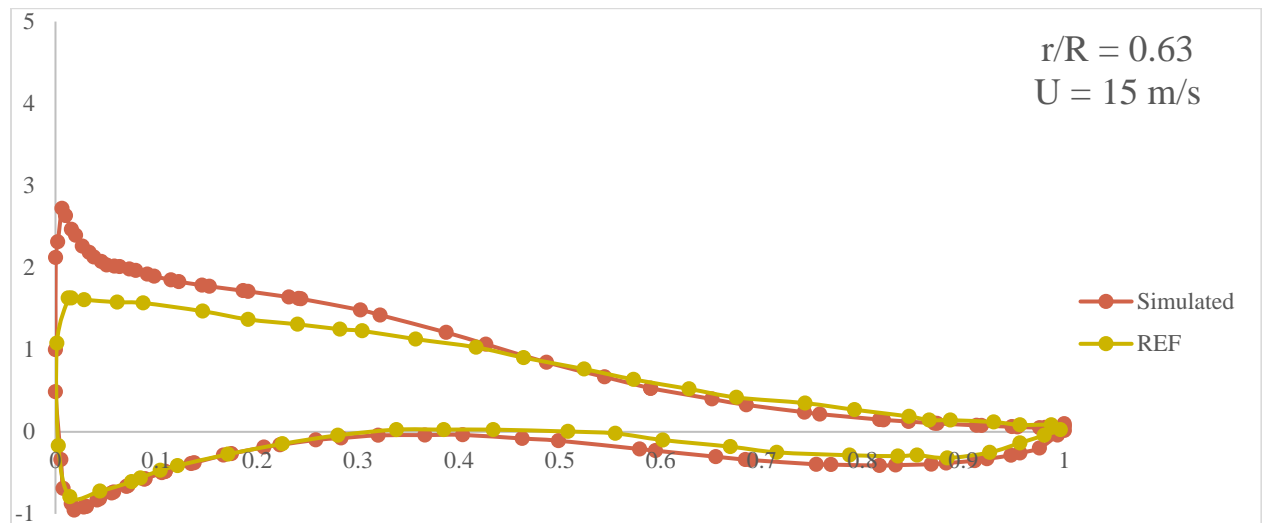Figure 18 continued

(b)

(c)
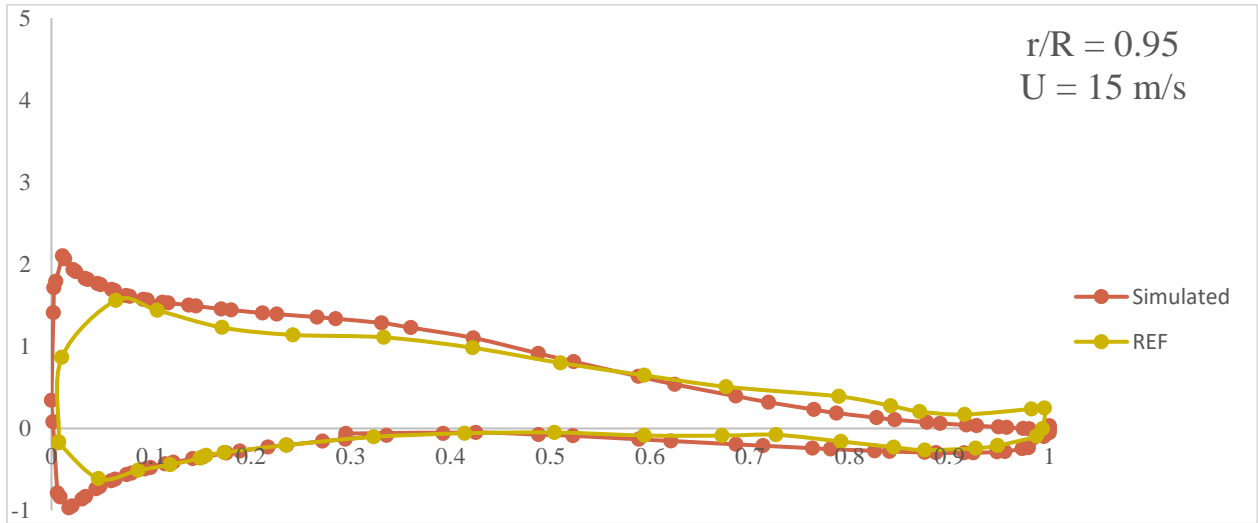
(a)

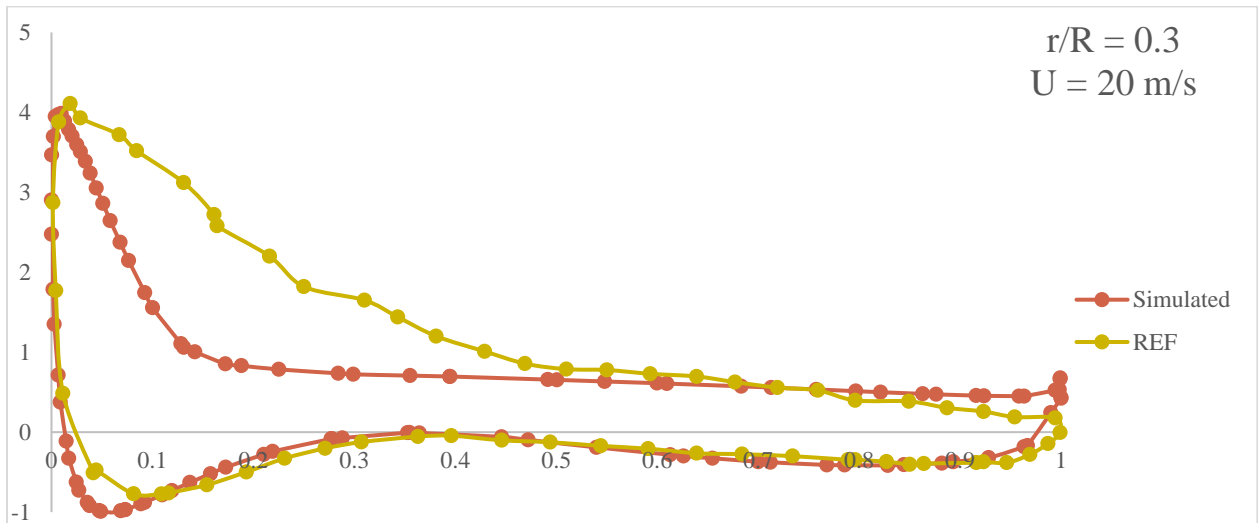
(b)

Figure 19. Pressure coefficient under U = 15 m/s

Figure 19 continued

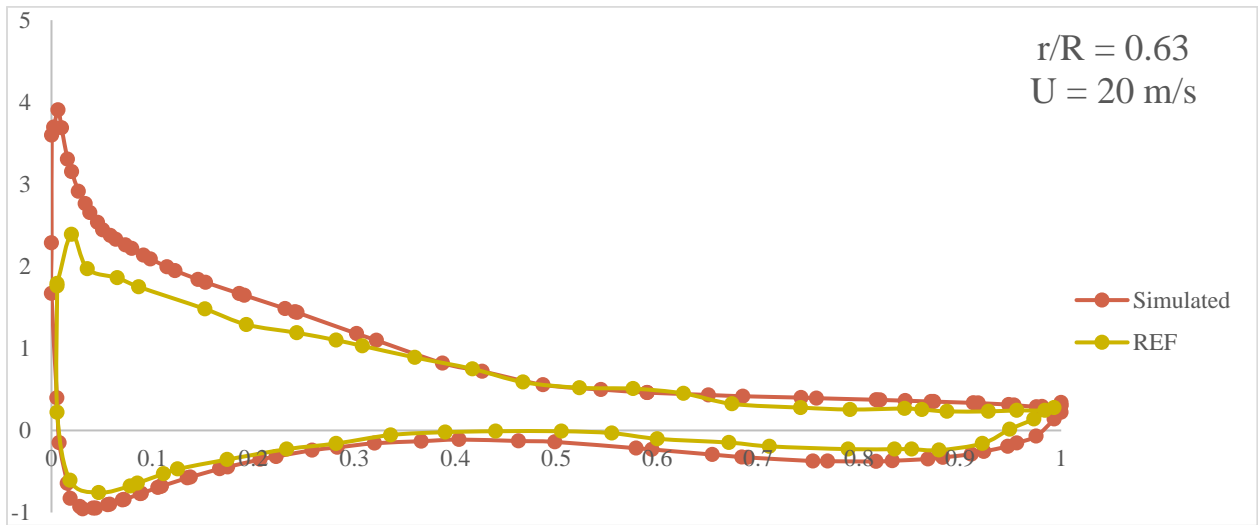(c)
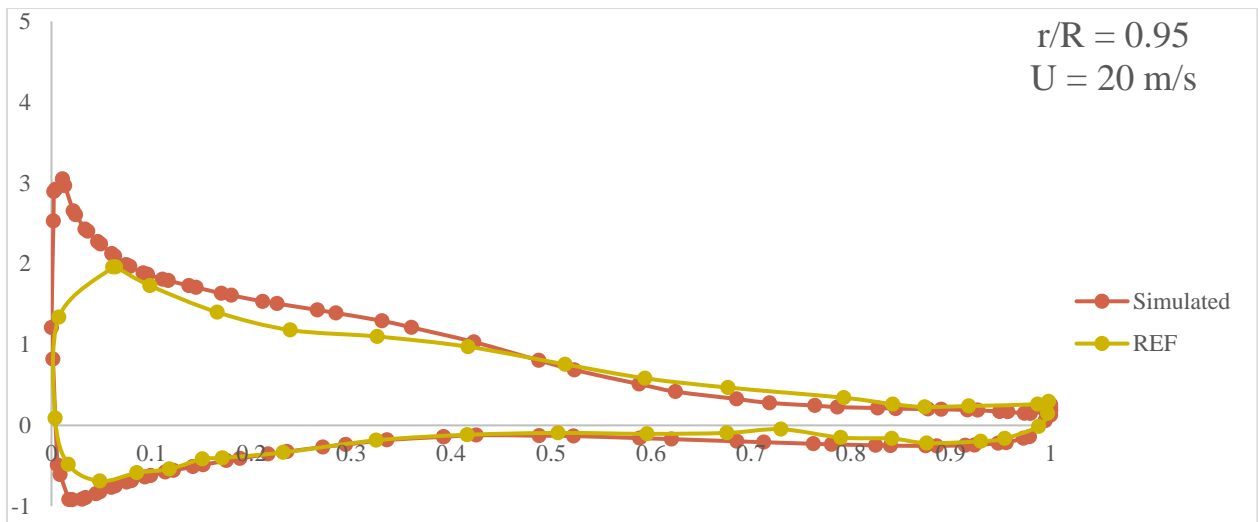

(a)

Figure 20. Pressure coefficient under U = 20 m/s
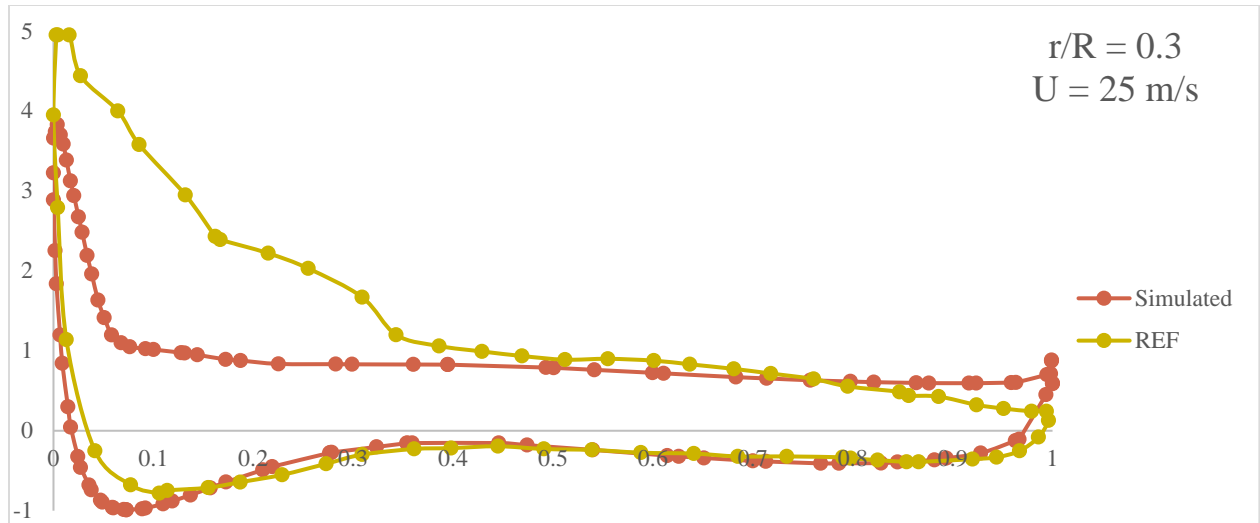
Figure 20 continued

(b)

(c)

(a)
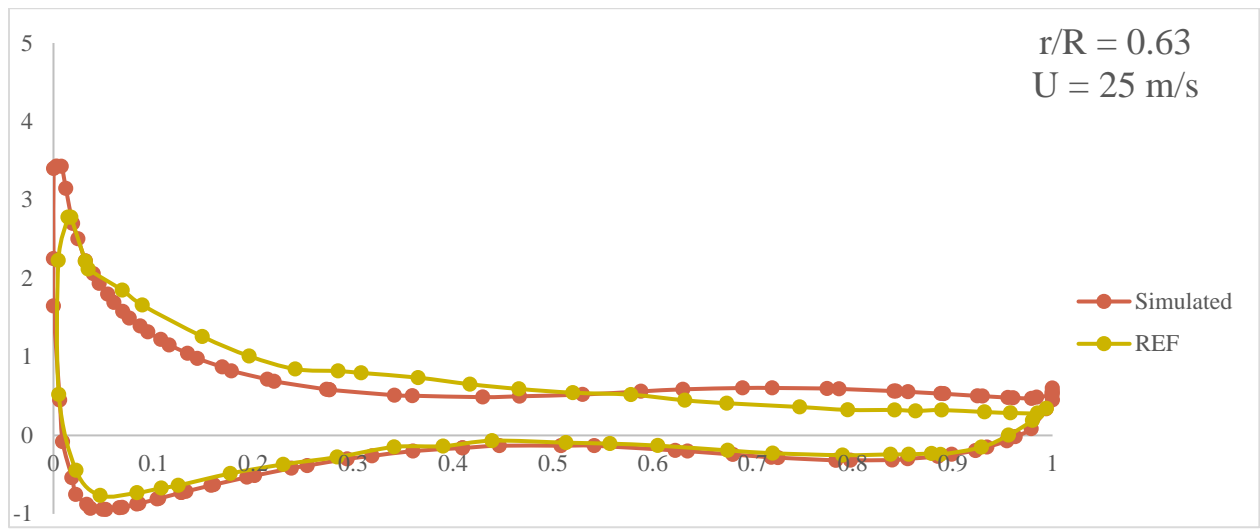
(b)

Figure 21. Pressure coefficient under U = 25 m/s

Figure 21 continued
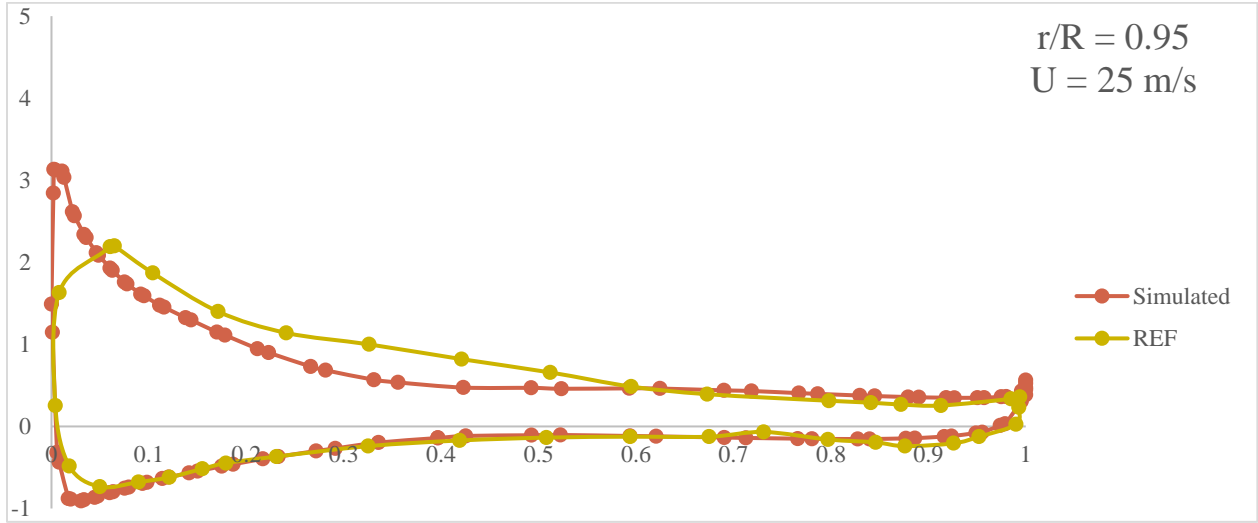
(c)

4.7   Torque and Thrust

As previously stated, this work has eight cases. In addition, the selected wind turbine was modelled under various input wind velocity conditions. The torque and thrust from different conditions were obtained, and the results are shown in Table 9. As has mentioned, 11.4 m/s is the rated wind inlet velocity. When the inlet wind velocity is less than 11.4 m/s, the rotation speed rises as the wind speed increases. When the inlet wind velocity exceeds 11.4 m/s, the rotation speed remains the same even if the wind speed keeps increasing. Moreover, it is obvious that when the inlet wind velocity grows, the corresponding torque and thrust increase as well.

The variation of the wind torque and thrust with wind velocity is exhibited in Table 9. With the rise of wind velocity, the thrust increases gradually, but the torque increases dramatically. The associated torque and thrust is exceptionally powerful, especially when the inlet wind velocity is larger than 11.4 m/s.

Table 10 displays the error of torque and thrust from the reference and NREL values, respectively. The torque error is less than the thrust error. Furthermore, the simulated results tend to be more consistent with the reference than the NREL results. It seems to be that the NREL thrust inaccuracy is as high as 27 percent, yet this may be explained by a lack of data for the thrust at 15, 20, and 25 m/s. The inaccuracy of thrust from reference is also rather high at wind velocities of 5,

8, and 9 m/s, but it declines with rising wind velocities. Overall, the simulated results are very consistent with the reference and NREL results.

Figure 22 demonstrates the variation of simulated torque with inlet wind speed. It is clear that the simulated results match the reference pretty well. When the wind speed does not exceed the specified wind velocity, which is 11.4 m/s, the curve from simulated results shows great consistency with the NREL results. When the inlet wind velocity exceeds the 11.4 m/s, there is not enough information from NREL. Figure 23 demonstrates the variation of thrust with wind speed.

Table 9. Rotor torque and thrust

Case	Wind speed(m/s)	Angular velocity (rpm)	Torque (kNm)	Thrust (kN)
1	4.00	7.18	305.39	126.00
2	5.00	7.39	644.68	180.08
3	8.00	9.16	2045.77	383.68
4	9.00	10.30	2596.96	486.49
5	11.40	11.89	4359.85	723.43
6	15.00	12.10	7743.53	954.61
7	20.00	12.10	10678.24	1083.75
8	25.00	12.10	10699.63	1142.40

Table 10. Error of torque and thrust

Wind speed (m/s)	Error of torque (%)		Error of thrust (%)	
	REF	NREL	REF	NREL
4.00	N/A	20.83	N/A	40.17
5.00	5.04	18.44	30.06	33.03
8.00	1.72	4.54	15.89	19.73
9.00	0.98	4.95	18.38	16.01
15.00	10.73	N/A	3.89	N/A
20.00	13.62		2.39	
25.00	1.92		2.13	
Average error (%)	5.67	12.19	12.12	27.24
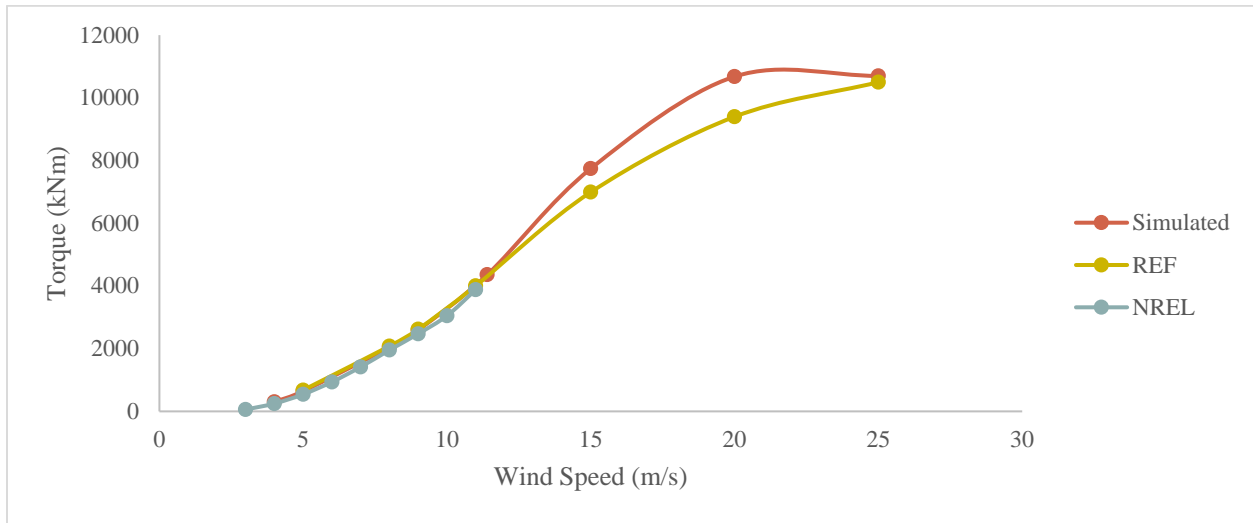
Figure 22. Torque versus wind speed
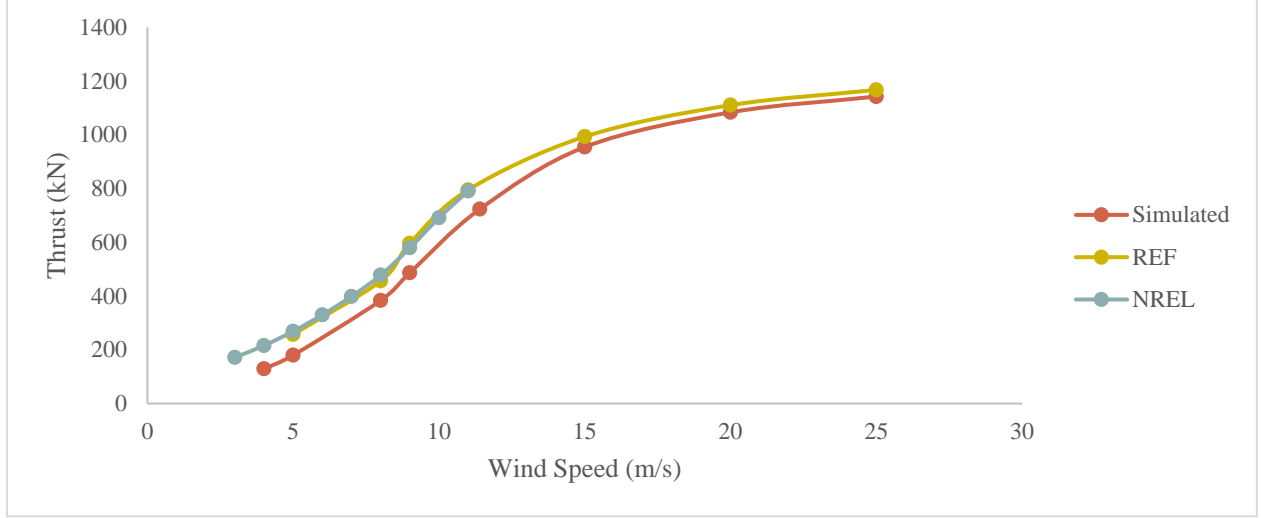
Figure 23. Thrust versus wind speed

4.8 Power Coefficient and Tip Speed Ratio

The coefficient of power is also a significant parameter in wind turbine study. It is expressed as the following equation.

$$C_p = \frac{T\omega}{1/2\, \rho\pi r^2 v^3} \tag{26}$$

In turbine design, the tip speed ratio is an essential parameter to consider, it can be expressed as

$$TSR = \lambda = \frac{\omega r}{v} \tag{27}$$

As is known that if a turbine rotates at a high speed, the turbine blades would perform like a solid wall to wind, and more turbulent could be generated. By contrast, if a turbine rotates at a low speed, the wind will pass through it, and less power could be generated. Both extreme conditions are not suitable for power generation. Therefore, finding the optimal TSR is essential for generating the maximum power.

Table 11 demonstrates the calculated power coefficient and TSR from 8 different cases. As the tip speed ratio reductions, the coefficient of power first increases to reach the peak and then goes down. Thus, the maximum power coefficient could be conducted. As is shown from the table, the maximum power coefficient is no more than 0.59, which refers to the Betz's limit.

Table 11. Power coefficient and tip speed ratio

Case	Tip Velocity (m/s)	Power Coefficient	TSR
1	47.30	0.47	11.83
2	48.67	0.52	9.734
3	60.25	0.504	7.53
4	67.7	0.505	7.52
5	78.25	0.48	6.86
6	79.7	0.38	5.31
7	79.7	0.22	3.99
8	79.7	0.11	3.19

In order to determine the maximum power coefficient and its corresponding optimal TSR. Figure 24 is generated. When the wind speed goes up, the curve of the power coefficient first has a strong tendency to increase. After the power coefficient reaches the peak, it goes down. In addition, when TSR is between 2 to 6, the power coefficient grows rapidly. While it is from 6 to 10, the rate of growth of the power coefficient slows down. The moment it is from 10 to 12, the power coefficient goes down. To conclude, for this work, the optimum tip speed ratio for maximum coefficient of power is around 9.
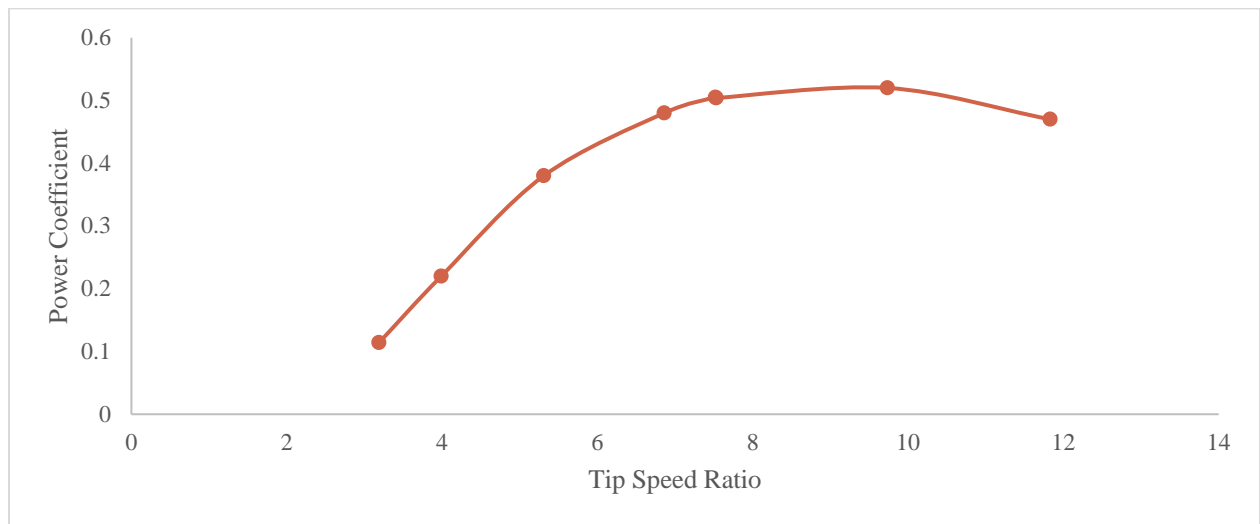
Figure 24. Power coefficient versus tip speed ratio

5. CONCLUSIONS AND FUTURE WORK

Numerical simulations have been conducted to the flow features and aerodynamic performances of the 5-MW offshore wind turbine.

The result form numerical simulation was first completed by mesh independent study. Comparing with the power coefficient at r/R = 0.63 under uniform 9 m/s from mesh 1,2, and 3 respectively, mesh 2 was selected as the appropriate mesh for this work.

The numerical simulation was validated by comparing the torque with others' work and reasonable agreement was observed. The error between simulated torque and other's results was calculated. The error calculated from Zhao and Jonkman's results are quite low, 3.17% and 4.96% respectively. The error is no more than 5%. Consequently, the current setting and model are feasible considering the low error.

Eight cases were created to investigate. Cases were designed with different wind speed. Four of eight cases were designed with wind speed that are lower than rated wind speed. one case was designed as the rated wind speed. And the inlet wind velocities of the rest three cases were over rated wind speed. Eight cases were simulated to obtain torque and thrust. The relationship between torque, thrust and wind speed was obtained. When the wind speed was relatively large, the corresponding thrust and torque were extremely large.

What's more, the flow field at y-z plane was visualized under three different velocity inlets. The first velocity inlet was a uniform and constant 9 m/s inlet. The other two were power law and linear velocity inlet. The common ground of three velocity inlet was that the velocity of the hub was 9 m/s.

Besides, the velocity profile at various selected location under different wind speed was presented. When the selected location is nearly to the turbine hub, the influence to the velocity profile is great. But, when the selected location is gradually far away from the blade, the influence of the wind turbine hub decreases. The recovery process of the velocity is presented. Compared the velocity profiles under different wind speed, it can be concluded that with the increase of the wind speed, the influence of the hub on velocity profile reduces.

In addition, limiting streamline was presented. It also indicated that the flow of the whole turbine blade was smooth except near the root area when the wind speed inlet was low. With the increase of the wind speed, the whole turbine blade was gradually occupied by vortices.

Moreover, the wake of the vortices which perform helically, intensely, and symmetrically were visualized. It was also concluded that with the growth of inlet wind velocity, the helical vortices could persist in a longer downstream distance. And the helical path with the increasing wind speed presents reasonable consistency with Zhao's work.

Furthermore, the pressure distribution along the blade was visualized and the pressure coefficient at 0.3, 0.63, 0.95 cross section under different wind speed conditions were obtained. It can be concluded that the pressure rises from the root to the tip of the blade. Also, the pressure at both windward side and suction side increases with the inlet wind speed increases. As for the pressure coefficient, the current results presented satisfied consistency with the reference work for the least error of the largest pressure coefficient was only around 0.92%. When the inlet wind velocity remained the same, the pressure coefficient at 0.3 cross section was larger than the others. It could be concluded that the leading edge of the airfoil contains more curvature than the trailing edge of the airfoil. The larger inlet velocity leads to a more evident curvature of the leading edge. When the wind speed was 25 m/s, the pressure coefficient was almost twice as the pressure coefficient under 5 m/s.

Last but not least, the relationship of power coefficient and TSR were investigated. When the wind speed increased, the coefficient of power first increased to reach a peak and then went down. When the power coefficient reached the peak, the corresponding optimal tip speed ratio is around 9.

In the future, pitched angle can be added to the wind turbine to reduce the thrust and torque. As has mentioned, the wind turbine endures vast velocity, pressure, thrust and torque when the inlet velocity is over 11.4 m/s. The wind turbine in this paper is considered as fixed, 6 DOF motion can be applied to wind turbine to investigate the aerodynamics as well.

REFERENCES

1. HES SOLOAR, Which energy source is most efficient, 2020
   https://hessolar.com/2020/01/which-energy-source-is-most-efficient/

2. E. Y. Bitar, R. Rajagopal, P. P. Khargonekar, K. Poolla and P. Varaiya, Bringing Wind Energy to Market, IEEE Transactions on Power Systems, Volume 27, 2012, Pages 1225-1235.

3. Wind Energy Foundation, 2014.
   http://www.windenergyfoundation.org/about-wind-energy/history

4. A. Zervos, Renewables 2017, Global Status Report Tech. rep., Paris, 2017.

5. S. Sawyer, L. Fried, S. Shukla, Q. Liming, Global Wind Report 2016-Annual Market Update Tech. rep. GWEC, 2016.

6. Y. Kumar, J. Ringenberg, S. S. Depuru, V. K. Devabhaktuni, J. Lee, E. Nikolaidis, B. Andersen, A. Afjeh, Trends and enabling technologies, Renewable and Sustainable Energy Reviews, Wind energy, Volume 53, 2016, Pages 209-224.

7. F. Wenehenubun, A. Saputra, H. Sutanto, An Experimental Study on the Performance of Savonius Wind Turbines Related With The Number Of Blades, Energy Procedia, Volume 68, 2015, Pages 297-304.

8. G. Y. Huang, Y. C. Shiah, C. J. Bai, W.T. Chong, Experimental study of the protuberance effect on the blade performance of a small horizontal axis wind turbine, Journal of Wind Engineering and Industrial Aerodynamics, Volume 147, 2015, Pages 202-211.

9. M. Talavera, F. Shu, Experimental study of turbulence intensity influence on wind turbine performance and wake recovery in a low-speed wind tunnel, Renewable Energy, Volume 109, 2017, Pages 363-371.

10. A. J. Coulling, A. Goupee, A. Robertson, J. M. Jonkman, H. J. Dagher, Validation of a FAST semi-submersible floating wind turbine numerical model with DeepCwind test data, Journal of Renewable and Sustainable Energy, Volume 5, 2013.

11. H. Shin, S. Cho, K. J. Jung, Model test of an inverted conical cylinder floating offshore wind turbine moored by a spring-tensioned-leg, International Journal of Naval Architecture and Ocean Engineering, Volume 6, Issue 1, 2014, Pages 1-13.

12. F. Duan, Z. Q. Hu, J.M. Niedzwecki, Model test investigation of a spar floating wind turbine, Marine Structures, Volume 49, 2016, Pages 76-96.

13. N. Troldborg, G. C. Larsen, H. A., Madsen, K. S. Hansen, J. N. Sørensen, R. Mikkelsen, Numerical simulations of wake interaction between two wind turbines at various inflow conditions, Wind Energy, Volume 14, 2011, Pages 859-876.

14. P. Cheng, Y. Huang, D. Wan, A numerical model for fully coupled aero-hydrodynamic analysis of floating offshore wind turbine, Ocean Engineering, Volume 173, 2019, Pages 183-196.

15. H. Zhou, D.C. Wan, Numerical investigations on the aerodynamic performance of wind turbine: downwind versus upwind configuration, J. Mar. Sci. Appl., Volume 14, 2015, Pages 61-68.

16. P. Cheng, D.C. Wan, C.H. Hu, Unsteady aerodynamic simulations of floating offshore wind turbines with overset grid technology Proceedings of the Twenty-sixth International Ocean and Polar Engineering Conference Rhodes, Greece, 2016.

17. J.M. Jonkman, S. Butterfield, W. Musial, G. Scott, Definition of a 5-MW Reference Wind Turbine for Offshore System Development National Renewable Energy Laboratory, Colorado, 2009.

18. F. Blaabjerg and K. Ma, Wind Energy Systems, Proceedings of the IEEE, Volume 105, 2017, Pages 2116-2131.

19. C. Wang, Computational Fluid Dynamic Simulation for an Offshore Wind Turbine, Master of Science (MS), Thesis, Mechanical Engineering and Mechanics, Lehigh University, Sep 2011.

20. C. Lienard, R. Boisard, C. Daudin, Aerodynamic Behavior of a Floating Offshore Wind Turbine, AIAA Journal, 2020, Pages 1-13.

21. T. Tran, D. H. Kim, J. Song, Computational Fluid Dynamic Analysis of a Floating Offshore Wind Turbine Experiencing Platform Pitching Motion, Energies, 2014, Pages 5011-5026.

22. H. Lee, D. J. Lee, Effects of platform motions on aerodynamic performance and unsteady wake evolution of a floating offshore wind turbine, Renewable Energy, Volume 143, 2019, Pages 9-23.

23. B. Dose, H. Rahimi, I. Herráez, B. Stoevesandt, J. Peinke, Fluid-structure coupled computations of the NREL 5 MW wind turbine by means of CFD, Renewable Energy, Volume 129, Part A, 2018, Pages 591-605.

24. W. C. Zhao, P. Cheng, and D. C. Wan, Numerical Computation of Aerodynamic Performances of NREL Offshore 5-MW Baseline Wind Turbine, The Eleventh ISOPE Pacific/Asia Offshore Mechanics Symposium, Shanghai, China, October 2014.

25. O. Y. Dong, J. K. Oh, predicting wind turbine blade loads and aeroelastic response using a coupled CFD–CSD method, Renewable Energy, Volume 70, 2014, Pages 184-196.

26. P. I. Aquino, Offshore Wind Energy, Simulating Local Offshore Wind Turbine, Master of Science (MS), Thesis, Mechanical & Aerospace Engineering, Old Dominion University, 2018.

27. N. Zhou, J. Chen, D.E. Adams, S. Fleeter, Influence of inflow conditions on turbine loading and wake structures predicted by large addy simulations using exact geometry, Wind Energy, 2016, Volume 19, Pages 803-824.

28. D. Zhao, N. Han, E. Goh, J. Cater, A. Reinecke, Chapter 5 - Offshore wind turbine aerodynamics modelling and measurements, Wind Turbines and Aerodynamics Energy Harvesters, Academic Press, 2019, Pages 373-400.

29. P. J. Moriarty, A. C. Hansen, AeroDyn theory manual, Colorado, 2005.